 doi:10.20944/preprints202109.0363.v2

Article

Modelling the heating process at transient and steady state of an In Situ Tape Laying Machine Head

Jhonny de Sá Rodrigues [1,*], Paulo Teixeira Gonçalves [1], Luis Pina [1] and Fernando Gomes de Almeida [2]

[1] Institute of Science and Innovation in Mechanical and Industrial Engineering (INEGI) Rua Dr. Roberto Frias, 4200-465 Porto, Portugal
[2] LAETA-INEGI, Faculty of Engineering, University of Porto, Rua Dr. Roberto Frias, s/n, 4200-465 Porto, Portugal
* Correspondence: jsrodrigues@inegi.up.pt

Abstract: As use of composite materials increases, the search for suitable automated processes gains relevance to guarantee production quality by ensuring uniformity of the process, minimizing the amount of generated scrap and reducing time and energy consumption. Limitations on production by traditional means such as hand lay-up, vacuum bagging and in-autoclave methods, tend not to be as efficient when the size and shape complexity of the part being produced increases, motivating the search for alternative processes such as the Automated Tape Laying (ATL). This work aims to describe the process of modelling and simulating a composite ATL with in situ consolidation by characterizing the machine elements, using the finite differences method in conjunction with energy balances, in order to create a digital twin of the process for further control design. The modelling approach implemented is able to follow the process dynamics when changes to the heating element are imposed as well as to predict the composite material temperature response, making it suitable to work as a digital twin of a production process using an ATL machine.

Keywords: Automatic Fiber Laying; Thermoplastic composites; Process simulation; Digital twin

1. Introduction

The search for more efficient and automated manufacturing processes for composite materials has found that the automated tape laying (ATL) process with in-situ consolidation for thermoplastic laminates is a good alternative to reduce material scrap, and increase manufacturability of complex geometries by out of autoclave processes [1–4].

This process requires a machine mainly composed by a heating source and a compaction mechanism in order to raise the composite temperature, guaranteeing the quality of the final part by ensuring that all the laid composite layers have been welded among themselves [5]. The main parameters that affect the quality of the final product are the temperature and the compaction roll pressure at the nip point [3,6]. The temperature is the most critical parameter to be controlled in order to reduce defects such as voids or delamination.

The heating process is the most critical stage, reaching the necessary composite temperature ensures a good bonding condition between the layers [7,8]. Inadequate temperature exposures of the thermoplastic matrix may cause degradation of the material and residual thermal stresses [2,9–11], making the final part defective and unable to meet the required performance.

Most modelling works of a heating head for the tape laying process that can be found in the literature, use lasers as heat sources [12–14] due to its controlled power delivery at a fixed wavelength and localized region. The way the heat source is pointed to the surface has a significant effect on the heating process due to the material surface reflection of the incoming energy, making the study of where to aim a laser beam, a relevant parameter as presented by [15] that relates the composite surface irregularities with its optical properties for a defined wavelength range.

Other studies using similar heat sources, study the temperature distribution by measuring the temperature just before the nip point using thermal cameras [16] and analysing the results for three different power values of the heat source. [4] proposes a

Citation: Rodrigues, J.; Gonçalves, P.; Pina, L.; Almeida, F. Title. *Preprints* **2021**, *1*, 0. https://doi.org/

Received:
Accepted:
Published:

 doi:10.20944/preprints202109.0363.v2

model using lasers to heat a set of thinner composite tapes, in order to study the influence of the tapes width on the overall heating process when the machine has to follow a non straight path.

Another heat source for this process are hot gas torches [14,17], where the heat transfer into the composite depends mainly on the convection coefficient computed using empirical correlations.

Independently of the heat source, all the models share the same phenomenological problem, that is, understanding the temperature response of the composite material during the process. The majority of the authors focus their works on numerical and experimental studies of the problem assuming constant process parameters like heat power and feed velocity, without considering the use of control strategies to improve the overall process by adjusting its parameters.

Another common characteristic of the models proposed in literature is related to their mathematical approach, using a three dimensional heat exchange as proposed by [18], which implies a high computational cost, that increases when the model results are used in combination with resin cure models as proposed by [19]. A simplified model was proposed by [20], using a hot air gun as heating source in which a 1.5D thermal approach is used; this model does not take into account the variations of the material properties with temperature. On the other hand, an analytical model was developed by [21], which relates process parameters such as laser beam power, process speed and mold temperature, regardless of the geometrical characteristics of the material being processed. This analytical approximation makes assumptions such as uniform heat flux exposition, no heat loss to the environment and constant thermophysical properties.

This work focuses in the development of a digital twin model for an automated tape laying (ATL) machine. The model takes into account the heat source, the composite material, the compaction roll and the surroundings as an enclosure, to study the temperature distribution along the material under different process conditions. The mathematical model is 1.5 dimensional as both the material and the reflector thickness are modelled with only one element in that direction. The thermo-optical properties of the elements with its temperature dependence were also considered within the infrared range, to obtain an accurate description of the process response.

In Section 2 are described the ATL machine head components. Section 3 presents the 1.5 dimensional mathematical model for the components described at the previous section, emphasising the radiation heat exchange model which involves optical and temperature dependant properties as well as their spatial distribution, it is also presented the mathematical model for the material the machine processes. Section 4 presents the thermal properties equations, as function of temperature, for the machine head elements. Section 5 presents the composite material to be used in terms of thermal and optical properties; it also presents the equation solver method to simulate the ATL process and it is described the strategy to measure the ATL process variables needed to feed the mathematical model. Section 6 presents the model validation by comparing the obtained measurements of the ATL process variables with the results calculated using the mathematical model.

2. The ATL Machine Head

The main components of the machine head assembly, numbered from 1 to 5 in Figure 1, are: **1** a material feeder, consisting on an unwinding mechanism that keeps the material straight along its pathway through the heating section; **2** a heat source, consisting on an infrared lamp and **3** a back plate that acts as a reflector; **4** an optical temperature sensor to measure the material temperature; **5** a compaction roll in which interior circulates a fluid at a controlled temperature that presses the heated material against **6** a mold.

Preprints (www.preprints.org) | NOT PEER-REVIEWED | Posted: 25 November 2021 doi:10.20944/preprints202109.0363.v2

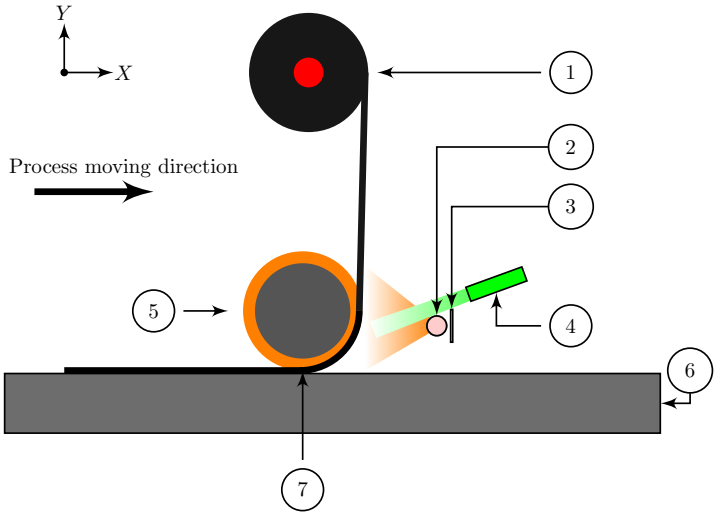

Figure 1. Machine head assembly. **(1)** material feeder. **(2)** heating element. **(3)** reflector. **(4)** optical temperature sensor. **(5)** compaction roll. **(6)** mold. **(7)** nip point.

The goal of the machine head is to create a laminate by heating up a continuous material tape to a temperature above its melting point, ensuring that when the material gets to the nip point, Figure 1, it will weld to a previous laid material layer, or the case for the first layer against the mold, it will follow the mold shape.

2.1. Infrared Heating Element

The infrared heater in the machine head assembly consists on a tungsten filament coil heated by an electric current that serves as the emitter. This emitter is surrounded by a quartz glass envelope. This quartz glass acts as an enclosure containing an inert gas to prevent filament oxidation at high temperatures as well as small amounts of halogen to inhibit the evaporation of tungsten via the halogen cycle.

To maintain the atmosphere inside the quartz envelope the current is passed through a pair of Molybdenum foil pads, ensuring the gas chamber seal to the outside atmosphere, for an increased service life. Figure 2 shows the heating element assembly.

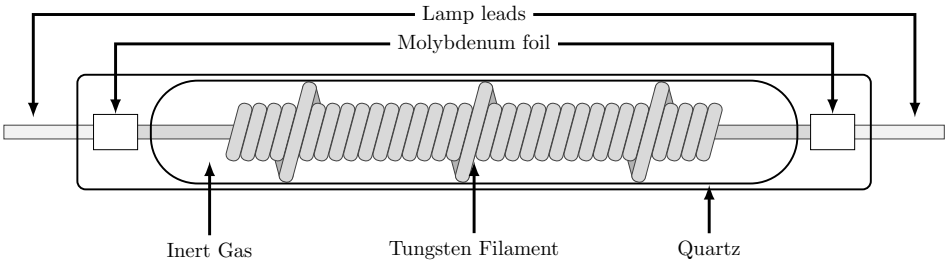

Figure 2. Heating element and its cross section

2.2. Compaction roll

The compaction roll is a cylinder that rotates with the motion of the entire machine head assembly while applying a fixed amount of pressure on top of the new material layer and the previous laid one, or mold surface for the case of the first laid material, ensuring a contact bonding between the two surfaces at the nip point. To avoid any damage to the heated material by the cylinder, a 5 mm coating of silicone rubber from Silex [22] covers the 100 mm diameter aluminium cylinder, preventing it from sticking to the material matrix during the process. On the other hand, to avoid overheating of the compaction roll silicon cover, a fluid is circulated through the metal housing of the cylinder to control its temperature, that according to the silicon manufacturer can go up to a maximum of 300 °C.

 doi:10.20944/preprints202109.0363.v2

2.3. Material feeder

The material feeder consists on a cylinder with a tension mechanism that ensures the material roll placed around it, to be always in tension while is being fed towards the compaction roll.

3. 1.5D Mathematical model for the ATL heating process

As given in the previous section the ATL head is composed mainly by an infrared lamp as a heating element with an aluminum back plate as a radiation reflector and a consolidation roll pressing down the heated material against the mould. The process involves two main phenomenons namely: the heating process to achieve the adequate consolidation temperature in the incoming material, and the consolidation process itself.

In this work the focus is given to the heating process of the incoming material because it is the most critical for process quality [8,11,23,24]. Both the reflector and the material will be modelled using a single element along its thickness. For the reflector, as its main function is to redirect the heating energy towards the material, it is not relevant to know the temperature distribution along its thickness; a compensation factor is implemented for heat losses due to convection at the surface facing the composite material and at the opposite surface. For the material, its thickness is significantly smaller than its length, so a temperature gradient along its thickness is negligible; hence, a 1.5D heat transfer model of the ATL head is proposed to develop a process digital twin allowing to run simulations and design proper control strategies.

Figure 1 presents the layout of the machine head assembly. It moves horizontally, parallel to the heated mold, and the material is fed vertically to the compaction roll which changes its orientation to horizontal when the nip point is reached. This makes the material feed velocity to match, the machine head assembly velocity. The other assembly elements such as the infrared lamp, the reflector, the compaction roll and the optical temperature sensor move horizontally along with the machine head.

Understanding the relative movements between the machine head components and the material is relevant as it determines the selection of the appropriate correlation for estimating the convection coefficients.

Figure 3 shows a schematic of the simplified model of the ATL presented in the previous section. The curved path was simplified to a straight line, where $y_{convection}$ corresponds to the region before reaching the roll, y_{roll} corresponds to the curved path in contact with the roll with its equivalent length and y_{mold} corresponds to the region after the nip point.

Preprints (www.preprints.org) | NOT PEER-REVIEWED | Posted: 25 November 2021 doi:10.20944/preprints202109.0363.v2

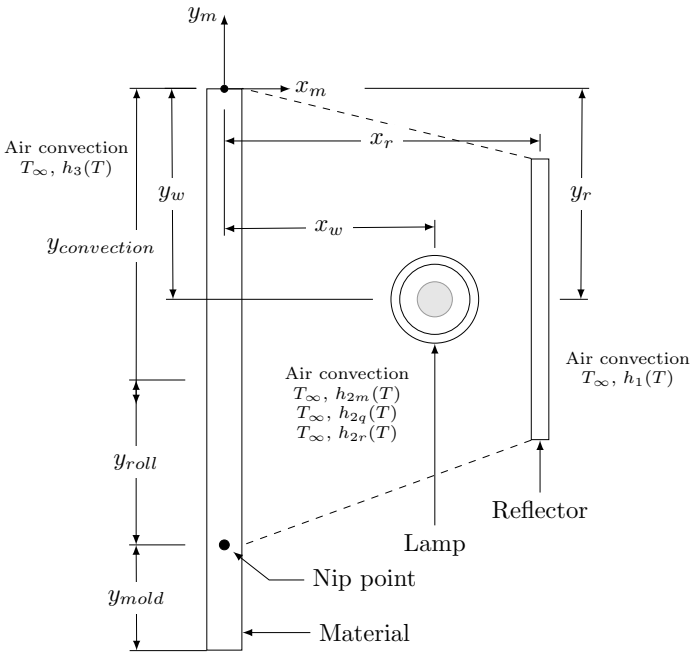

Figure 3. 1.5D model schematic.

The ATL model involves an open cavity radiation problem where the heat emitted by the lamp and reflected by the reflector is used to increase the temperature of the entering material tape before it reaches the nip point. Heat loss to the ambient by convection and radiation also takes place and will be considered in the modelling.

Figure 3 shows three different zones of heat exchange over the material: The first one, delimited by $y_{convection}$ has radiation from the lamp and convection to the surrounding air, which convection coefficient depends on air temperature, air flow velocity and direction. The second one, delimited by y_{roll} involves heat exchange from radiation, convection and conduction to the compaction roll. The third zone, delimited by y_{mold} involves only conduction to both, compaction roll and mold.

To develop the proposed model each one of the components is analyzed as follows.

3.1. Heater

The heater element is a halogen lamp composed by a tungsten filament enclosed by a cylindrical quartz envelope filled with neon gas. A simplification of the lamp geometry is presented in Figure 4 where a concentric arrangement of the components is proposed [25]. Figure 4a presents a front view of the lamp model as the tungsten is modeled as a solid cylinder of length l_w and diameter d_{coil} as a simplification of its spiral construction (Figure 4c), and the quartz envelope as a hollow cylinder of length l_q, thickness t_q (Figure 4a) and external diameter d_l (Figure 4b).

Preprints (www.preprints.org) | NOT PEER-REVIEWED | Posted: 25 November 2021 doi:10.20944/preprints202109.0363.v2

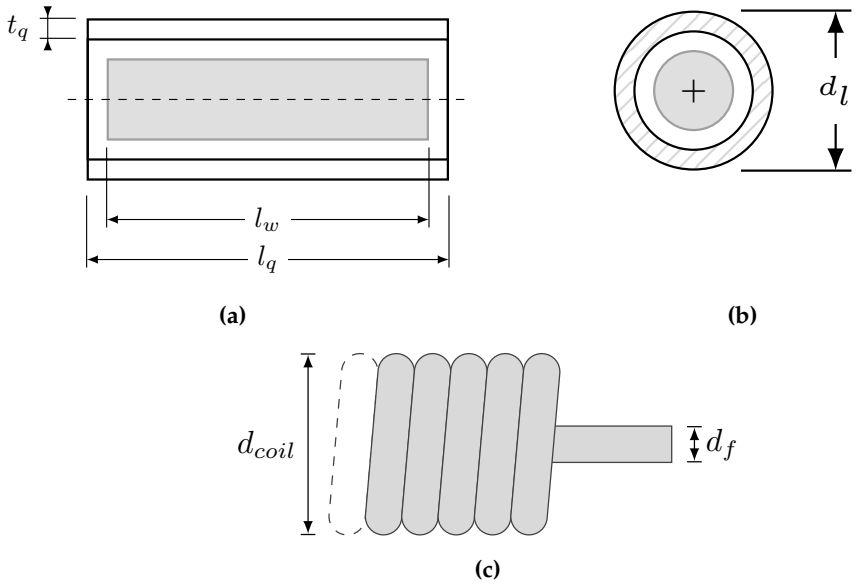

Figure 4. Lamp model. (**a**) Lamp model front view. (**b**) Lamp model cross section. (**c**) Filament model

3.1.1. Tungsten filament

The tungsten filament is considered as an homogeneous element with an internal heat generation given by its electrical resistance which is a function of temperature T_f, and the applied voltage, that exchanges heat with the neon by conduction and with the inner face of the quartz lamp by radiation. No convection between the filament and the neon is considered because of the low value for the Grashof number as suggested by [25], indicating conduction as the predominant phenomena for this particular heat exchange process. Then the heat transfer model used for the tungsten filament is the energy balance given in (1) [26,27],

$$m_f \, cp_f(T_f) \, \frac{dT_f}{dt} = \left(P_{el} - Q_{r,f} - Q_{c,n}\right) \tag{1}$$

where:

m_f:	Filament mass, [kg]
T_f:	Filament temperature, [K].
$cp_f(T_f)$:	Filament specific heat (temperature dependent), $\left[\frac{\text{J}}{\text{kg·K}}\right]$.
P_{el}:	Electric power, [W].
$Q_{r,f}$:	Radiation heat, [W].
$Q_{c,n}$:	Conduction heat, [W].

The electric power of the resistance, can be expressed using (2),

$$P_{el} = \frac{U_e^2}{R(T_f)} \tag{2}$$

where U_e stands for the applied voltage, and the electrical resistance $R(T_f)$ can be expressed as a function of the resistivity, filament length l_f and filament cross sectional area a_f (3).

$$R(T_f) = r_w(T_f) \frac{l_f(T_f)}{a_f(T_f)} \tag{3}$$

3.1.2. Neon

The neon has a very low thermal capacitance compared to the tungsten and quartz, hence its thermal capacitance is neglected. Accordingly, the neon transfers heat from the tungsten to the lamp internal surface by conduction. Taking advantage of the cylindrical

Preprints (www.preprints.org) | NOT PEER-REVIEWED | Posted: 25 November 2021 doi:10.20944/preprints202109.0363.v2

configuration, the heat conducted by the neon can be approximated using the cylindrical solution for radial conduction (4) given in [26].

$$Q_{c,n} = 2 \cdot \pi \cdot l_q \cdot K_n(T_n) \cdot \frac{\left(T_f - T_q\right)}{ln\left(\frac{d_L}{d_{coil}}\right)} \tag{4}$$

where:

$Q_{c,n}$: Conduction heat, [W]
$K_n(T_n)$: Neon conductivity (temperature dependent), $\left[\frac{\mathrm{W}}{\mathrm{m \cdot K}}\right]$.
T_n: Neon mean temperature $\left(\frac{T_f - T_q}{2}\right)$, [K]
T_q: Quartz lamp temperature, [K]
d_L: Lamp diameter, [m]
d_{coil}: Filament coil diameter, [m]
l_q: Lamp length, [m]

3.1.3. Quartz glass envelope

The quartz envelope is considered to have a constant temperature T_q across the thickness because it has a small thickness. The energy balance for the envelope is given in (5).

$$m_q \cdot cp_q(T_q) \cdot \frac{dT_q}{dt} = \left(Q_{r,f} + Q_{c,n} - Q_{r,q} - h_{2q} A_q \left(T_q - T_\infty\right)\right) \tag{5}$$

where:

m_q: Quartz cylinder mass, [kg]
$cp_q(T_q)$: Quartz specific heat, $\left[\frac{\mathrm{J}}{\mathrm{kg \cdot K}}\right]$
$Q_{r,f}$: Incoming radiation heat, [W]
$Q_{r,q}$: Outgoing radiation heat, [W]
$Q_{c,n}$: Conduction heat, [W]
h_{2q}: Convection coefficient, $\left[\frac{\mathrm{W}}{\mathrm{m^2 K}}\right]$
A_q: Quartz surface area, $[\mathrm{m}^2]$
T_∞: Air Temperature inside the radiation cavity, [K]

Some of the data required for the lamp simulation is expressed in Table 1 from measurements performed on a series of lamps.

Table 1. Measurements for the lamp characteristics

Lamp Property	Measured value
Lamp length	189 mm $\pm$ 0.34 mm
Lamp diameter	10 mm $\pm$ 0.19 mm
Lamp resistance (at 23 $^\circ$ C)	9.6 $\Omega \pm 6.41 \cdot 10^{-6}$ Ω
Filament diameter	0.41 mm $\pm$ 0.0038 mm
Filament coil diameter	2.89 mm $\pm$ 0.0039 mm
Filament coil length	290 mm $\pm$ 0.37 mm
Filament mass	5.2019 g $\pm$ 0.00048 g
Lamp glass mass	13.8780 g $\pm$ 0.00049 g

3.2. Reflector

The lamp reflector is considered as a thin metal sheet with constant temperature across thickness t_r and is modelled as a 1.5D finite volume problem along its width W_r. The reflector is transferring heat with the ambient air at its right hand side surface $(T_\infty, h_1(T))$,

Preprints (www.preprints.org) | NOT PEER-REVIEWED | Posted: 25 November 2021 doi:10.20944/preprints202109.0363.v2

transferring heat with the internal air in the cavity $(T_\infty, h_{2r}(T))$, and reflecting radiation heat from the lamp. An energy balance over a reflector cell of volume V_r is given in (6) taking into account its surfaces S_r for heat exchange.

$$\frac{\partial}{\partial t}\int_{V_r}\rho_r\cdot cp_r(T_r)cdotT_r\cdot dV_r=\int_{\partial V_r}k_r(T_r)\cdot(\nabla T_r\cdot\hat{n})\cdot dS_r + \int_{\partial V_r}q''_{rad,r}\cdot dS_r+\int_{\partial V_r}q''_{conv,r}\cdot dS_r \tag{6}$$

where:

ρ_r:	Reflector material density, [kg/m^3]
T_r:	Reflector temperature, [K]
$cp_r(T_r)$:	Reflector specific heat (temperature dependent), $\left[\frac{\text{J}}{\text{kg}\cdot\text{K}}\right]$
$k_r(T_r)$:	Reflector conductivity (temperature dependent), $\left[\frac{\text{W}}{\text{m}\cdot\text{K}}\right]$
$q''_{rad,r}(T_r)$:	Radiation heat, $\left[\frac{\text{W}}{\text{m}^2}\right]$
$q''_{conv,r}(T_r, T_\infty)$:	Convection heat $\left[\frac{\text{W}}{\text{m}^2}\right]$

A finite volume technique is used to discretize the lamp reflector geometry as shown in Figure 5. The application of the energy balance to each reflector cell gives the cell equation (7a) for the unknown cell temperature, with the coefficients given by (7b) through (7e). The material properties inside the volume cell are constant and are evaluated at the nodal temperature.

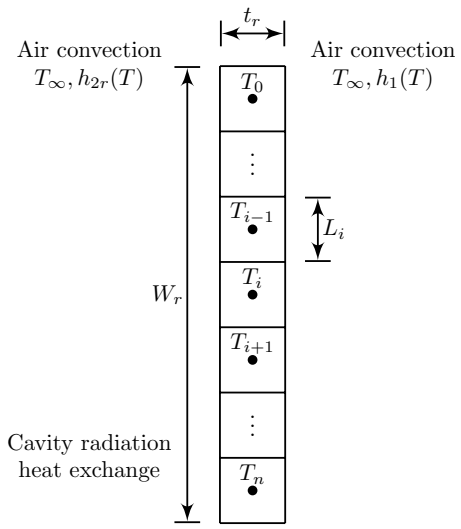

Figure 5. 1.5D model for the reflector

$$\dot{T}_r=(A_r)T_{r-1}-(2A_r+B_{r,1}+B_{r,2})T_r+(A_r)T_{r+1}+(B_{r,1})T_{\infty,1}+(B_{r,2})T_{\infty,2} +(C_r)\ q''_{rad,r}(T_r) \tag{7a}$$

with:

Preprints (www.preprints.org) | NOT PEER-REVIEWED | Posted: 25 November 2021 doi:10.20944/preprints202109.0363.v2

$$A_r = \frac{k_r(T_r)}{\rho_r \cdot cp_r(T_r) \cdot L_r^2} \tag{7b}$$

$$B_{r,1} = \frac{h_1}{\rho_r \cdot cp_r(T_r) \cdot t_r} \tag{7c}$$

$$B_{r,2} = \frac{h_{2r}}{\rho_r \cdot cp_r(T_r) \cdot t_r} \tag{7d}$$

$$C_r = \frac{1}{\rho_r \cdot cp_r(T_r) \cdot t_r} \tag{7e}$$

where:

r:	Reflector cell number 0,1,...,n
L_r:	Length of reflector cell, [m]
t_r:	Reflector thickness, [m]
T_∞:	Air temperature, [K]
$h_1(T_r, T_\infty)$:	External convection coefficient, $\left[\frac{\mathrm{W}}{\mathrm{m^2 \cdot K}}\right]$
$h_{2r}(T_r, T_\infty)$:	Internal convection coefficient, $\left[\frac{\mathrm{W}}{\mathrm{m^2 \cdot K}}\right]$

The lateral conditions for the reflector are defined as adiabatic (8a) (8b) due to $W_r \gg t_r$, making the heat exchange in those surfaces negligible in comparison with the heat exchange of the remaining surfaces.

$$\left.\frac{\partial T}{\partial y}\right|_{y=0} = 0 \tag{8a}$$

$$\left.\frac{\partial T}{\partial y}\right|_{y=W_r} = 0 \tag{8b}$$

3.3. Material

The material fiber tape is placed at a velocity U, over a mold at constant temperature T_{mold}, while it is heated by the lamp. The material domain begins at the section where the material is feed (Z_1), exchanging heat by radiation and convection, followed by the section Z_2 where heat transfer by conduction also occurs due to the contact between the material and the compaction roll, and ends with Z_3 at which the consolidation point its located.

The tape is considered as a thin sheet with constant temperature across its thickness and supplied at a constant temperature T_0. The energy balance for a cell volume V_m of the material tape is given in (9),

$$\begin{aligned}
&\frac{\partial}{\partial t}\int_{V_m} \rho_m \cdot cp_m(T_m) \cdot T_m \cdot dV_m = \int_{\partial V_m} k_m(T_m) \cdot (\nabla T_m \cdot \hat{n}) \cdot dS_m \\
&- \int_{\partial V_m} \rho_m \cdot cp_m(T_m) \cdot T_m \cdot (U \cdot \hat{n}) \cdot dS_m \\
&+ \int_{\partial V_m} q''_{rad,m} \cdot dS_m + \int_{\partial V_m} q''_{conv,m} \cdot dS_m + \int_{\partial V_m} q''_{cond,m} \cdot dS_m
\end{aligned} \tag{9}$$

where:

Preprints (www.preprints.org) | NOT PEER-REVIEWED | Posted: 25 November 2021 doi:10.20944/preprints202109.0363.v2

ρ_m: Composite material density, [kg/m^3]
T_m: Material Temperature, [K]
$cp_m(T_m)$: Composite specific heat (temperature dependent), $\left[\frac{\text{J}}{\text{kg}\cdot\text{K}}\right]$
$k_m(T_m)$: Composite conductivity (temperature dependent), $\left[\frac{\text{W}}{\text{m}\cdot\text{K}}\right]$
$q''_{rad,m}(T_m)$: Radiation heat, $\left[\frac{\text{W}}{\text{m}^2}\right]$
$q''_{conv,m}(T_m, T_\infty)$: Convection heat, $\left[\frac{\text{W}}{\text{m}^2}\right]$
$q''_{cond,m}(T_m, T_{mold})$: Conduction heat, $\left[\frac{\text{W}}{\text{m}^2}\right]$

A finite volume technique is used to represent the tape geometry, Figure 6, and the application of the energy balance to each tape cell gives the cell equation (10a) for the unknown cell temperature using the coefficients given by (10b) through (10h).

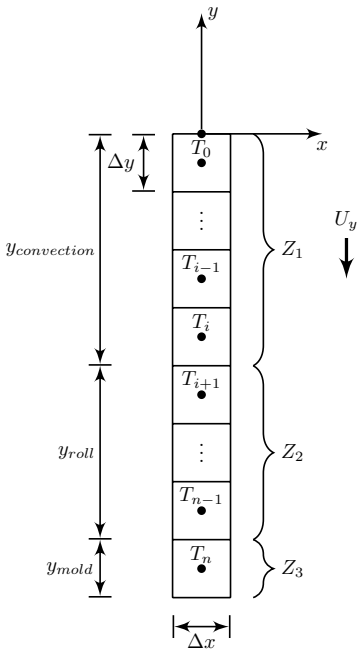

Figure 6. 1.5D material model

$$\begin{aligned}\dot{T}_m = {} & \left(A|_{Z_1,Z_2,Z_3}\right)\cdot T_{m+1} + \left(A|_{Z_1,Z_2,Z_3} + B|_{Z_1,Z_2,Z_3}\right)\cdot T_{m-1} \\ & + \left(-2\,A|_{Z_1,Z_2,Z_3} - C1|_{Z_1,Z_2} - C2|_{Z_1} - D1|_{Z_2} - D2|_{Z_3}\right)\cdot T_m \\ & + C1|_{Z_1,Z_2}\cdot T_\infty + C2|_{Z_1}\cdot T_\infty + D1|_{Z_2}\cdot T_{roll} + D2|_{Z_3}\cdot T_{mold} \\ & + D3|_{Z_1,Z_2}\cdot q''_{rad}\end{aligned} \tag{10a}$$

with:

Preprints (www.preprints.org) | NOT PEER-REVIEWED | Posted: 25 November 2021 doi:10.20944/preprints202109.0363.v2

$$A = \frac{k_m(T_m)}{\rho_m \cdot cp_m(T_m) \cdot \Delta y^2} \tag{10b}$$

$$B = \frac{U}{\Delta y} \tag{10c}$$

$$C1 = \frac{h_{2m}}{\rho_m \cdot cp_m(T_m) \cdot \Delta x} \tag{10d}$$

$$C2 = \frac{h_3 m}{\rho_m \cdot cp_m(T_m) \cdot \Delta x} \tag{10e}$$

$$D1 = \frac{1}{\rho_m \cdot cp_m(T_m) \cdot \Delta x \cdot R_{roll}} \tag{10f}$$

$$D2 = \frac{1}{\rho_m \cdot cp_m(T_m) \cdot \Delta x \cdot R_{mold}} \tag{10g}$$

$$D3 = \frac{1}{\rho_m \cdot cp_m(T_m) \cdot \Delta x} \tag{10h}$$

where:

m:	Material cell number 0, 1,..., n
R_{mold}:	Composite wall resistance for heat conduction between mold and the material, [$m^2 \cdot K/W$]
R_{roll}:	Composite wall resistance for heat conduction between compaction roll and the material, [$m^2 \cdot K/W$]
q''_{rad}:	Net radiation from the surfaces involved in the heat exchange process, [W/m^2]
h_{2m}:	Convection coefficient for the material surface facing the heating element, [W/m^2]

The terms (10b) through (10h) are evaluated into (10a) taking into account each material section Z_i as shown in Figure 6, allowing to obtain the corresponding boundary conditions for the cell. After evaluating all the terms for all the material cells, a system of differential equations is built to compute the new material temperatures.

At section Z_1 the material arrives at an initial temperature $T_0 = T_\infty$ where convection ($C1$, $C2$) and radiation ($D3$) are the main heat exchange phenomena. At this section the convection, which relation is defined using the inside enclosure air properties (T_∞, h_{2m}), and the radiation phenomena are added to the balance to complete the relation. The radiation term added comes from an energy balance further discussed in this work; at section Z_2 radiation ($D3$), convection ($C1$) and conduction ($D1$) are the heat exchange phenomena present; at section Z_3 the material is located between the compaction roll and the mold, this means that conduction ($D1$, $D2$) is the main heat exchange phenomena occurring between the compaction roll and the mold simultaneously. For this model, the temperature of the nip point is located at the material cell T_n, and the previously laid material temperature is modelled assuming constant value of T_{mold}. The terms R_{mold} and R_{roll} are explained in the following section.

The boundary condition related to the y axis at the first material cell is represented using (11a), and the last material cell, in the same y axis, is represented using (11b).

$$T|_{y=0} = T_0 \tag{11a}$$

$$\frac{\partial T}{\partial y} = 0 \tag{11b}$$

Preprints (www.preprints.org) | NOT PEER-REVIEWED | Posted: 25 November 2021 doi:10.20944/preprints202109.0363.v2

3.4. Compaction roll and mold

The compaction roll is used to press the incoming material, once heated, against the mold or the previously laid material during consolidation. It consists on a hollow aluminum cylinder in which interior circulates water at a constant temperature to avoid mechanical damage to the seals and bearings. The exterior of the cylinder is covered by a layer of solid high temperature silicone rubber Silex GP60THT [22].

The model strategy to simulate the heat exchange process between the compaction roll and the material is to use a combination between composite hollow cylinder with 1D radial conduction for the compaction roll internal fluid, the aluminium structure and the rubber layer, and 1D conduction of a plane wall approximation for the material [26], becasue the thickness of the material is thinner than the the rubber layer or even the aluminium structure of the cylinder, making the relation $ln\left(\frac{D_{roll}/2 + t_{rubber} + \Delta x}{D_{roll}/2 + t_{rubber}}\right) \approx 0$, where D_{roll} is the compaction roll diameter without the rubber layer, t_{rubber} is the thickness of the rubber layer and Δx is the thickness of the material.

For the case presented at section Z_2 in Figure 6 the heat exchange phenomena are convection, radiation and conduction. The energy balance for conduction to the compaction roll at this section can be obtained from Figure 7a, where the heat exchange by conduction is mathematically expressed as an array of resistors connected in series relations (12a) and (12b).

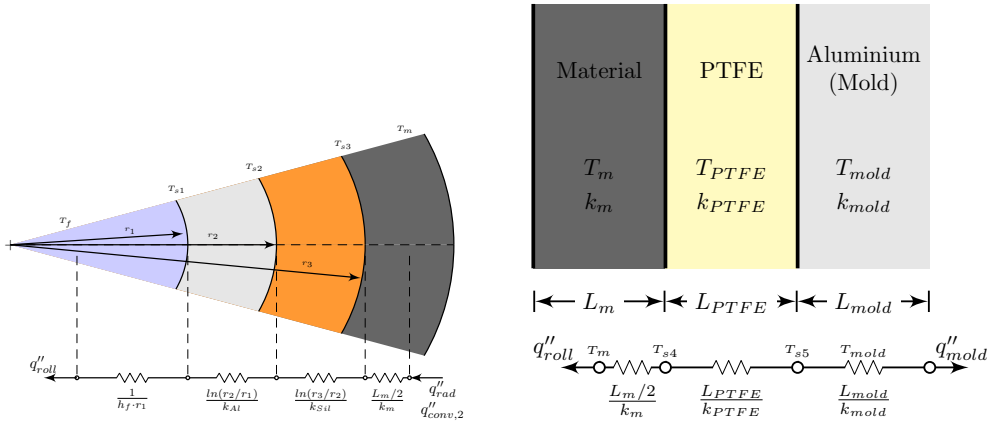

(a) **(b)**

Figure 7. Composite wall for the heat conduction balance. (**a**) Composite wall model for the compaction roll 1D Compaction roll D_3. (**b**) 1D Compaction roll in section D_4

$$R_{roll} = \frac{1}{h_f \cdot r_1} + \frac{ln(r_2/r_1)}{k_{Al}} + \frac{ln(r_3/r_2)}{k_{Sil}} + \frac{L_m/2}{k_m} \tag{12a}$$

$$R_{roll} = \frac{ln(r_2/r_1)}{k_{Al}} + \frac{ln(r_3/r_2)}{k_{Sil}} + \frac{L_m/2}{k_m} \tag{12b}$$

From Figure 7a the term R_{roll} is deduced taking into account the convection coefficient of the internal fluid giving relation (12a) and for a constant internal temperature it can be deduced the relation (12b).

At section Z_3 in Figure 6, the scheme for the energy balance involves conduction through the mold, as presented in Figure 7b. For the mold it is considered a film of Polytetrafluoroethylene (PTFE) acting as a mold releasing agent between the laid material and the mold; from Figure 7b the term R_{mold} gives the relation (13)

$$R_{mold} = \frac{L_m/2}{k_m} + \frac{L_{PTFE}}{k_{PTFE}} + \frac{L_{mold}}{k_{mold}} \tag{13}$$

Preprints (www.preprints.org) | NOT PEER-REVIEWED | Posted: 25 November 2021 doi:10.20944/preprints202109.0363.v2

3.5. Radiation

Radiation as heat transfer has been well studied when gray surfaces participate inside an enclosure, it is described in several text books [26–29] and by several researchers [25,30–32]. For this work, the general enclosure is described in Figure 3 where the reflector, the lamp and the material are involved, and the dashed lines represent a hypothetical surface acting as the surroundings to close the enclosure. In order to simplify calculations, the radiation flux problem is modeled as a two dimensional system allowing to calculate the heat flux per unit of area; equations (7a) and (10a) can be solved using the radiation heat input expressed in $[W/m^2]$. It is worth to mention that the view factors for two dimensional problems are well studied and equations have been developed to simplify calculations [27–29,32,33], these equations are discussed further in this work.

This work also considers another enclosure, in this case the lamp, which is composed as described in section 3.1 by a tungsten filament inside a quartz glass envelope. In this enclosure, the filament exchanges heat, mostly in form of radiation with the inner surface of the quartz envelope. At the same time, part of this radiation is also exchanged with the external glass surface due to the glass being a transparent media; this is fundamental when defining the Radiosity balance among the involved surfaces in the general enclosure.

To calculate the radiation energy of a gray surface, first, the radiation energy for an equivalent black body is calculated using the Planck's Law (14a), then a correcting factor, particular for each surface nature and temperature, is applied to transform the black body radiation into a gray body radiation. Those correcting factors are further discussed.

$$E_b = \int_0^\infty \frac{C_1}{\lambda^5 \cdot \left[e^{\left(\frac{C_2}{\lambda \cdot T}\right)} - 1 \right]} d\lambda \tag{14a}$$

with:

$$C_1 = 2 \cdot \pi \cdot h \cdot c_0^2 = 3.742 \cdot 10^8 \left[\frac{W \cdot \mu m^4}{m^2} \right] \tag{14b}$$

$$C_2 = \frac{h \cdot c_0}{k_b} = 1.439 \cdot 10^4 \ [\mu m \cdot K] \tag{14c}$$

where:

- λ: Wavelength, [μ m]
- T: Absolute temperature of the black body, [K]
- h: Universal Planck constant, $6.626 \cdot 10^{-34}$ [J · s]
- k_b: Boltzmann constant, $1.381 \cdot 10^{-23}$ [J/K]
- c_0: Speed of light in vacuum, $2.998 \cdot 10^8$ [m/s]

For this work, the radiation energy is focused on the infrared region of the spectrum, narrowing the calculation region between λ_1 and λ_2 (0.4 μm and 20 μm respectively), then the total energy for a black body is obtained using (15) from Planck's Law (14a).

$$E_{\lambda,b} = \int_{\lambda_1}^{\lambda_2} \frac{C_1}{\lambda^5 \cdot \left[e^{\left(\frac{C_2}{\lambda \cdot T}\right)} - 1 \right]} d\lambda \tag{15}$$

As the energy calculation depends of the wavelength, and the integration is required along a finite band of wavelengths, the numerical solution is achieved evaluating the first 10 terms of the infinite series (16a), where σ stands for the Stefan-Boltzmann Constant, $5.670 \cdot 10^{-8} \left[\frac{W}{m^2 \cdot K^4} \right]$. By dividing the studied wavelength interval into 20 equally distributed

Preprints (www.preprints.org) | NOT PEER-REVIEWED | Posted: 25 November 2021 doi:10.20944/preprints202109.0363.v2

evaluation domains it is possible to obtain a good approximation while improving the calculation time in comparison with numerical integration routines [27,30].

$$E_b(T) = \sigma \cdot T^4 \left[\frac{15}{\pi^4} \left(\sum_{n=1}^{\infty} \frac{e^{-n\cdot\xi_2}}{n} \left(\xi_2^3 + \frac{3\xi_2^2}{n} + \frac{6\xi_2}{n^2} + \frac{6}{n^3} \right) \right. \right. \\ \left. \left. - \sum_{n=1}^{\infty} \frac{e^{-n\cdot\xi_1}}{n} \left(\xi_1^3 + \frac{3\xi_1^2}{n} + \frac{6\xi_1}{n^2} + \frac{6}{n^3} \right) \right) \right] \tag{16a}$$

with:

$$\xi_2 = \frac{h \cdot c_0}{k_b \cdot \lambda_2 \cdot T} \tag{17a}$$

$$\xi_1 = \frac{h \cdot c_0}{k_b \cdot \lambda_1 \cdot T} \tag{17b}$$

3.5.1. Radiative fluxes

To define the radiative balance, an identification of the surfaces involved is presented in Figure 8, as well as the Radiosity, J_i, and Irradiation, G_i, notation for each surface with its respective indices.

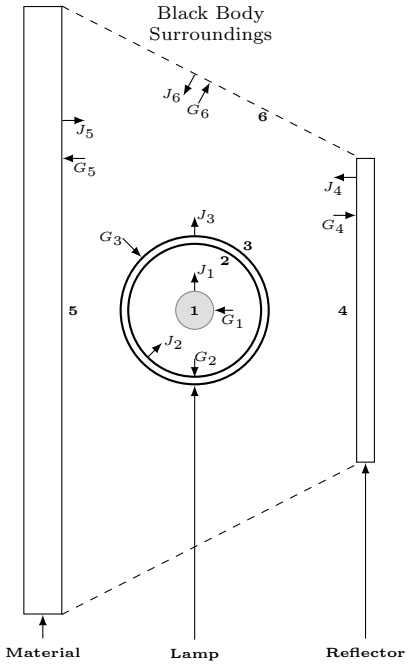

Figure 8. Surface identification. **1** Tungsten filament surface. **2** Internal quartz glass surface. **3** External quarts glass surface. **4** Reflector surface. **5** Material surface. **6** Equivalent surroundings surface

The boundary condition labeled as 6 is defined as a black body representing a surface that closes the enclosure. This allows to determine the net radiating heat transfer (18) using relation (19) for each surface.

$$q_i'' = J_i - G_i, \tag{18}$$

$$J_{\lambda,i} = r_{\lambda,i} \cdot G_i + \tau_{\lambda,i} \cdot G_{\lambda,i} + \varepsilon_{\lambda,i} \cdot \sigma \cdot T_i^4 \tag{19}$$

Preprints (www.preprints.org) | NOT PEER-REVIEWED | Posted: 25 November 2021 doi:10.20944/preprints202109.0363.v2

The first step is consider the Radiosity for each surface, giving the set of relations (20a) through (20f):

$$J_{\lambda,1} = r_{\lambda,1} \cdot G_{\lambda,1} + \varepsilon_{\lambda,1} \cdot E_{\lambda,1} \tag{20a}$$
$$J_{\lambda,2} = r_{\lambda,2} \cdot G_{\lambda,2} + \tau_{\lambda,3} \cdot G_{\lambda,3} + \varepsilon_{\lambda,2} \cdot E_{\lambda,2} \tag{20b}$$
$$J_{\lambda,3} = r_{\lambda,3} \cdot G_{\lambda,2} + \tau_{\lambda,2} \cdot G_{\lambda,2} + \varepsilon_{\lambda,3} \cdot E_{\lambda,3} \tag{20c}$$
$$J_{\lambda,4} = r_{\lambda,4} \cdot G_{\lambda,4} + \varepsilon_{\lambda,4} \cdot E_{\lambda,4} \tag{20d}$$
$$J_{\lambda,5} = r_{\lambda,5} \cdot G_{\lambda,5} + \varepsilon_{\lambda,5} \cdot E_{\lambda,5} \tag{20e}$$
$$J_{\lambda,6} = r_{\lambda,6} \cdot G_{\lambda,6} + \varepsilon_{\lambda,6} \cdot E_{\lambda,6} \tag{20f}$$

as suggested in [25,33]. In generic matrix form, for n involved surfaces, the relation is given by (21):

$$\left[J_{\lambda,j}\right]_{n\times 1} = [r]_{n\times n}\left[G_{\lambda,j}\right]_{n\times 1} + [\tau]_{n\times n}\left[G_{\lambda,j}\right]_{n\times 1} + [\varepsilon]_{n\times n}\left[E_{\lambda,j}\right]_{n\times 1} \tag{21}$$

where relations (20b) and (20c), which are related to the quartz envelope, contemplates the transmission $\tau_{\lambda,i}$ between both inner and outer surfaces due to the glass being a semitransparent media. The term $r_{\lambda,i}$ refers to the reflectivity of the body and the term $\varepsilon_{\lambda,i}$ refers to the emissivity; all surfaces are considered diffuse gray bodies. Relation (20f) refers to the surroundings considered as black body, acting as a heat sink as the temperature is known and kept constant along time, according to literature [25,27,28,34] it is defined $r_{\lambda,6} = 0$.

The second step is to consider the irradiation balance on the different surfaces by using (22):

$$A_i \cdot G_{\lambda,i} = \sum_{j=1}^{n}\left[A_j \cdot J_{\lambda,j} \cdot F_{j-i}\right] \tag{22}$$

where F_{j-i} is the view factor from surface j to surface i, A_i and A_j are the areas of surfaces i and j respectively.

From the view factor reciprocity property (23), the expression (22) can be written as (24a), or in its compact form (24b).

$$A_i \cdot F_{i-j} = A_j \cdot F_{j-i} \tag{23}$$

$$A_i \cdot G_{\lambda,i} = A_i \cdot J_{\lambda,1} \cdot F_{i-1} + A_i \cdot J_{\lambda,2} \cdot F_{i-2} + A_i \cdot J_{\lambda,i} \cdot F_{i-i} + \cdots + A_i \cdot J_{\lambda,n} \cdot F_{i-n} \tag{24a}$$
$$G_{\lambda,i} = \sum_{j=1}^{n} J_{\lambda,j} \cdot F_{i-j} \tag{24b}$$

In matrix form, for n involved surfaces the relation can be written as (24c):

$$\left[G_{\lambda,i}\right]_{n\times 1} = [F]_{n\times n}\left[J_{\lambda,j}\right]_{n\times 1} \tag{24c}$$

In order to solve this equation system, the equations (21) and (24c) are combined, leading to (25) enabling the irradiation computation.

$$\left[G_{\lambda,i}\right]_{n\times 1} = \left([I]_{n\times n} - [F]_{n\times n}\left([r]_{n\times n} + [\tau]_{n\times 1}\right)\right)^{-1}[F]_{n\times n}[\varepsilon]_{n\times 1}[E_{\lambda,i}]_{n\times 1} \tag{25}$$

Then, the results obtained using (25) are used into (21) to calculate the Radiosity $J_{\lambda,i}$. This allows the computation of the net radiative flux leaving each involved surface per

Preprints (www.preprints.org) | NOT PEER-REVIEWED | Posted: 25 November 2021 doi:10.20944/preprints202109.0363.v2

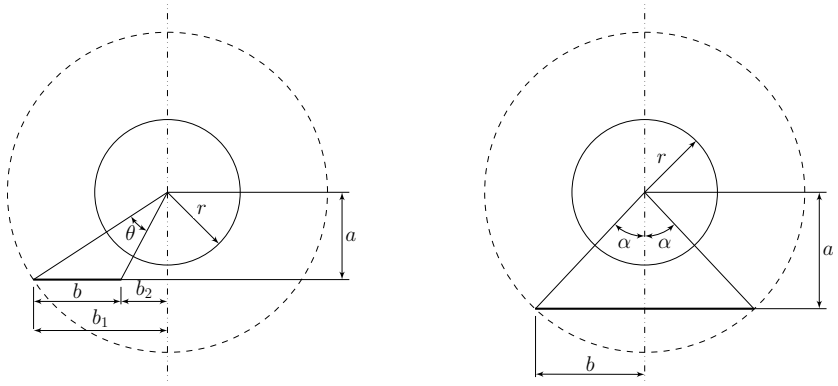

(a) **(b)**

Figure 9. View factor between a cylindrical surface and a plane surface. **(a)** Rectangle not aligned with the cylinder vertical center line. **(b)** Rectangle symmetrically aligned with the cylinder vertical center line.

unit area defined as (18) which are the boundary conditions needed to solve the lamp (1) (4) and (5), the reflector (7a) and the material (10a) temperatures.

3.5.2. View Factors

The view factors used in (22) through (25) are taken from literature [27–30,35], the view factor relations (26) and reciprocity (23).

$$\sum_{j=1}^{n} F_{i-j} = 1 \tag{26}$$

As mentioned before, the lamp is modeled as a solid tungsten cylinder inside a quartz glass envelope (enclosure), so the view factor for infinitely long concentric cylinders can be expressed as (27a), (27b) and (27c), which indices refer to the notation shown in Figure 8.

$$F_{1-2} = 1 \tag{27a}$$

$$F_{2-1} = \frac{d_{coil}}{d_l} \tag{27b}$$

$$F_{2-2} = 1 - F_{2-1} \tag{27c}$$

The view factor for an infinitely long cylinder to an infinitely long rectangle can be obtained using the scheme presented in Figure 9a, being the one presented in Figure 9b a particular case when $b_1 = b/2$.

The relation to calculate the different view factor values for the case between the lamp and the reflector, and the lamp and each material cell are expressed in (28a) and (28b), where the subscript *cyl.* refers to the outer lamp surface labeled as "3" in Figure 8 and the subscript *rect.* refers to the reflector labeled as 4 and the material labeled as 5 ain the same figure.

$$F_{cyl.-rect.} = \frac{1}{2 \cdot \pi}\left(tan^{-1}\frac{b_1}{a} - tan^{-1}\frac{b_2}{a}\right) \tag{28a}$$

$$F_{rect.-cyl.} = \frac{r}{b}\left(tan^{-1}\frac{b_1}{a} - tan^{-1}\frac{b_2}{a}\right) \tag{28b}$$

The view factors between two planar surfaces, in the 2D case, can be expressed using the Hottel's cross string method. Figure 10 shows the different components of this method. The values L_1, L_2, L_3, L_4, L_5 and L_6 are lengths, being L_1 and L_2 the surfaces involved in

Preprints (www.preprints.org) | NOT PEER-REVIEWED | Posted: 25 November 2021 doi:10.20944/preprints202109.0363.v2

the view factor and the remaining values distances between the edges of the surfaces, in this case the cells of the finite volume method.

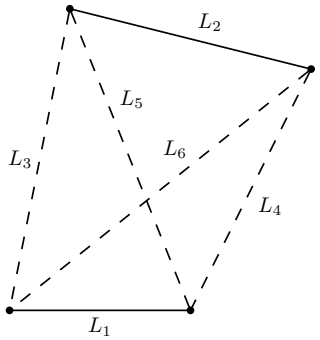

Figure 10. Two dimensional planar geometry. Hottel's method

The view factor using the Hottel's method is expressed as (29a) for the case $F_{L_1-L_2}$ and (29b) for the case $F_{L_2-L_1}$.

$$F_{1-2} = \frac{(L_5 + L_6) - (L_3 + L_4)}{2 \cdot L_1} \tag{29a}$$

$$F_{2-1} = \frac{(L_5 + L_6) - (L_3 + L_4)}{2 \cdot L_2} \tag{29b}$$

4. Properties

The properties of the elements involved in the heat exchange process are temperature dependant and they can be classified as thermal and optical properties, affecting directly the heat flux distribution model.

4.1. Thermal properties

In equations (1), (4) and (5) the specific heat of the tungsten, $cp_w(T_f)$, as well as the quartz, $cp_q(T_q)$, are needed. This data has been collected from literature [25,28,36] and summarized in (30a) and (30b) for the tungsten with a temperature range of 298 K $< T <$ 1900 K and 1900 K $< T <$ 3680 K respectively and for the quartz (30c) with a temperature range of 298 K $< T <$ 2000 K [28,37,38].

$$cp_w(T_f) = \frac{\left[23.9593 + 2.63968\frac{T_f}{10} + 1.25775\left(\frac{T_f}{10}\right)^2 - 0.25364\left(\frac{T_f}{10}\right)^3 - \frac{0.048407}{\left(\frac{T_f}{10}\right)^2}\right]}{183.84 \times 10^{-3}} \tag{30a}$$

$$cp_w(T_f) = \frac{\left[-22.5764 + 90.2798\left(\frac{T_f}{10}\right) - 44.2715\left(\frac{T_f}{10}\right)^2 + 7.1766\left(\frac{T_f}{10}\right)^3 - \frac{24.0974}{\left(\frac{T_f}{10}\right)^2}\right]}{183.84 \times 10^{-3}} \tag{30b}$$

$$cp_q(T_q) = \frac{\left[55.98 + 15.4 \times 10^{-3} \cdot T_q - \frac{14.1 \times 10^5}{T_q^2}\right]}{60.085 \times 10^{-3}} \tag{30c}$$

Also the tungsten resistivity and thermal conductivity of the Neon, both temperature dependant, are required. From [25] the data for the tungsten resistivity is given by (31) for a temperature range 300 K $< T <$ 3655 K and the conductivity for the Neon gas is given by (32) for a temperature range of 100 K $< T <$ 2500 K.

Preprints (www.preprints.org) | NOT PEER-REVIEWED | Posted: 25 November 2021 doi:10.20944/preprints202109.0363.v2

$$r_w(T_f) = -5.0134 \times 10^{-9} + 7.3070759 \times 10^{-11} \cdot T_f^{1.1796583} \tag{31}$$

$$k_{Ne}(T_{Ne}) = -3.6018021 \times 10^{-3} + 1.4290623 \times 10^{-3} \cdot T_{Ne}^{0.63362378} \tag{32}$$

Equation (7a) requires the specific heat of the reflector, $cp_r(T_r)$, which expression is presented in (33) for a temperature range of 298 K $< T <$ 933 K [36,39,40] and its thermal conductivity, $k_r(T_r)$, expressed in (34) for a temperature range of 250 K $< T <$ 800 K [41].

$$cp_r(T_r) = \frac{4.186 \cdot \left(4.94 + 2.96 \times 10^{-3} \cdot T_r\right)}{26.98154} \tag{33}$$

$$k_r(T_r) = 186.0219 + 0.327088 \cdot T_r - 6.069629 \times 10^{-4} \cdot T_r^2 + 3.101227 \times 10^{-7} \cdot T_r^3 \tag{34}$$

4.2. Optical properties

The optical properties needed by the system of equations (21) for each surface type are wavelength dependant. For general surfaces the relation among its optical properties is expressed by (35a), and for the case of opaque surfaces which have no transmissivity $\tau = 0$, the relation among its optical properties is expressed in (35b) [26,40].

$$r + \alpha + \tau = 1 \tag{35a}$$

$$\varepsilon \cong \alpha = 1 - r \tag{35b}$$

To estimate the optical properties of the opaque surfaces, the Maxwell electromagnetic wave theory gives the emissivity value (36a), that when used in (35b) leads to the reflectivity,

$$\varepsilon_{n,\lambda} = \frac{4 \cdot n}{n^2 + k^2 + 1 + 2 \cdot n} \tag{36a}$$

where n and k are given by equations (36b) and (36c) respectively:

$$n^2 = \frac{1}{2}\left(\sqrt{\left(\frac{\epsilon}{\epsilon_0}\right)^2 + \left(\frac{\lambda}{r_i \cdot 2 \cdot c_0 \cdot \epsilon_0}\right)^2} + \frac{\epsilon}{\epsilon_0}\right) \tag{36b}$$

$$k^2 = \frac{1}{2}\left(\sqrt{\left(\frac{\epsilon}{\epsilon_0}\right)^2 + \left(\frac{\lambda}{r_i \cdot 2 \cdot c_0 \cdot \epsilon_0}\right)^2} - \frac{\epsilon}{\epsilon_0}\right) \tag{36c}$$

with:

$\frac{\epsilon}{\epsilon_0}$: Relative material i permitivity
ϵ_0 : Vacuum permitivity $[\mathrm{F} \cdot \mathrm{m}^{-1}]$
r_i: Resistivity of element i, $[\Omega \cdot \mathrm{m}]$, for filament the resistivity is given by (31), for reflector the resistivity is given by (37) [41,42]

$$r_r = -1.1961 \times 10^{-8} + 1.5272 \times 10^{-10} \cdot T_r - 9.4257 \times 10^{-14} \cdot T_r^2 + 7.2288 \times 10^{-17} \cdot T_r^3 \tag{37}$$

For the tungsten filament the value for the relative permitivity is $\epsilon/\epsilon_0 = 1.000068$ and for the reflector $\epsilon/\epsilon_0 = 1.00000065$ [43].

Preprints (www.preprints.org) | NOT PEER-REVIEWED | Posted: 25 November 2021 doi:10.20944/preprints202109.0363.v2

The optical properties of the quartz glass envelope are gathered from specialized literature on the study of infrared dryers [33]; the the values of the quartz glass optical properties, for the range of wavelengths between 0.1 µm and 20.0 µm is shown in Table 2

Table 2. Optical properties for the quartz glass envelope [33]

L [µm]	ε	r	τ	L [µm]	ε	r	τ	L [µm]	ε	r	τ
0.1	0.05	0.05	0.90	1.4	0.04	0.07	0.89	3.75	0.23	0.05	0.72
0.2	0.05	0.05	0.90	1.6	0.03	0.06	0.90	4.0	0.36	0.04	0.60
0.3	0.05	0.05	0.90	1.8	0.02	0.07	0.91	4.5	0.65	0.03	0.32
0.4	0.05	0.05	0.90	2.0	0.01	0.08	0.91	5.0	0.90	0.03	0.07
0.5	0.05	0.05	0.90	2.2	0.01	0.06	0.93	6.0	0.97	0.03	0.00
0.6	0.05	0.05	0.90	2.4	0.02	0.06	0.92	7.0	0.96	0.04	0.00
0.7	0.06	0.05	0.89	2.6	0.01	0.07	0.92	8.0	0.92	0.08	0.00
0.8	0.06	0.05	0.89	2.8	0.02	0.07	0.91	9.0	0.63	0.37	0.00
0.9	0.05	0.06	0.89	3.0	0.05	0.05	0.90	10.0	0.74	0.26	0.00
1.0	0.05	0.06	0.89	3.25	0.03	0.06	0.91	11.0	0.89	0.11	0.00
1.2	0.05	0.07	0.89	3.5	0.04	0.06	0.90	>12.0	0.92	0.08	0.00

The emissivity value used in (20f) is $\varepsilon_\lambda = 1$ as surroundings are considered as black bodies.

4.3. Convection coefficients

For the convection parameters, needed for solving (5), (7a) and (10a), empirical correlations are used to estimate h_1, h_{2r}, h_{2q}, h_{2m} and h_3 [26]. Those correlations estimate an average convection coefficient for the air $\overline{h_i}$ by calculating an average Nusselt number Nu. The properties for the air at atmospheric pressure are computed at T_{film} (38) according to the information presented in literature [26].

$$T_{film} = \frac{T_i + T_\infty}{2} \tag{38}$$

To estimate h_1 the set of correlations (39a), (39b) and (39c) for perpendicular air flow were used, where the value U of the movement of the machine head is used to calculate the Reynolds number.

$$Re_{r1} = \frac{U \cdot W_r}{\nu(T_{film})} \tag{39a}$$

$$\overline{Nu_{r1}} = 0.228 \cdot Re_{W_r}^{0.731} \cdot Pr_{air}(T_{film})^{1/3} \tag{39b}$$

$$\overline{h_1} = \frac{\overline{Nu_{r1}} \cdot k_{air}(T_{film})}{W_r} \tag{39c}$$

For the left hand side of the reflector h_{2r}, the correlations for a vertical plane with free convection (40a), (40b) and (40c) were used,

Preprints (www.preprints.org) | NOT PEER-REVIEWED | Posted: 25 November 2021 doi:10.20944/preprints202109.0363.v2

$$\overline{Nu_{r2}} = \left\{ 0.825 + \frac{0.387 \cdot Ra_{r2}^{1/6}}{\left[1 + \left(0.492/Pr_{air}(T_{film})\right)^{9/16}\right]^{8/27}} \right\}^2 \tag{40a}$$

$$Ra_{r2} = \frac{g \cdot (1/T_{film}) \cdot (T_r - T_\infty) \cdot W_r^3}{\nu(T_{film}) \cdot \alpha(T_{film})} \tag{40b}$$

$$\overline{h_{2r}} = \frac{\overline{Nu_{r2}} \cdot k_{air}(T_{film})}{W_r} \tag{40c}$$

where $g = 9.807\ \mathrm{m/s^2}$.

For the lamp h_{2q}, the correlations for a cylinder with free convection were used (41a), (41b) and (41c). The position of the reflector relative to the lamp blocks the air flow due to the machine head assembly movement.

$$\overline{Nu_q} = \left\{ 0.60 + \frac{0.387 \cdot Ra_q^{1/6}}{\left[1 + \left(0.559/Pr_{air}(T_{film})\right)^{9/16}\right]^{8/27}} \right\}^2 \tag{41a}$$

$$Ra_q = \frac{g \cdot (1/T_{film}) \cdot (T_q - T_\infty) \cdot W_r^3}{\nu(T_{film}) \cdot \alpha(T_{film})} \tag{41b}$$

$$\overline{h_{2q}} = \frac{\overline{Nu_q} \cdot k_{air}(T_{film})}{d_L} \tag{41c}$$

For the case of h_{2m} and h_3, the same correlations are used (42a), (42b) and (42c) which consider an external air flow of velocity U parallel to the material surface due to the material motion relative to the air, that is assumed be at a quiescent state.

$$Re_m = \frac{U \cdot W_m}{\nu(T_{film})} \tag{42a}$$

$$\overline{Nu_m} = \frac{0.3387 \cdot Re_m^{1/2} \cdot Pr_{air}(T_{film})^{1/3}}{\left[1 + \left(0.0468/Pr_{air}(T_{film})\right)^{2/3}\right]^{1/4}} \tag{42b}$$

$$\overline{h_m} = \frac{\overline{Nu_m} \cdot k_{air}(T_{film})}{W_m} \tag{42c}$$

5. Materials and methods

5.1. Material description

As a case of study for the ATL process, the employed material is a carbon fiber reinforced Polyamide 6 tape from Toray with the commercial denomination Cetex TC910®, it is 50 mm width, 0.16 mm thickness, and has a fiber content of 60% [44].

5.1.1. Thermal properties

Equation (9) requires the material heat capacity as a function of temperature, $cp_m(T_m)$. An experimental procedure was performed according to ASTM E 1269-9901 [45] to material samples, giving the results shown in Figure 11 for a temperature range of 300 K $< T <$ 508 K.

Preprints (www.preprints.org) | NOT PEER-REVIEWED | Posted: 25 November 2021 doi:10.20944/preprints202109.0363.v2

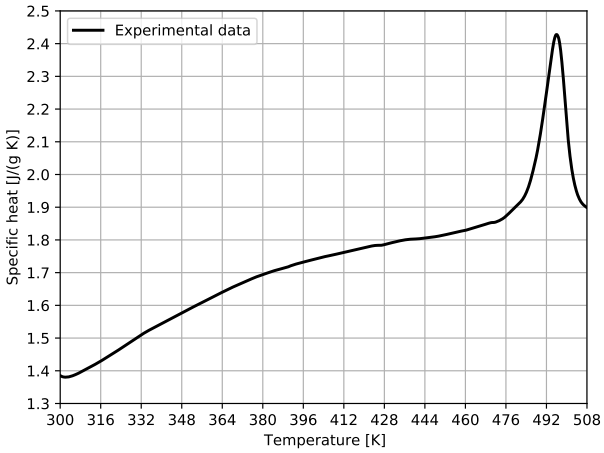

Figure 11. Specific heat for the composite material as a function of temperature.

Another property required in (9) is the material conductivity, $k_m(T_m)$. An in house procedure was used to determine this property as a function of temperature based on theoretical and practical works by [46], [47], [48] and [49]. The resulting data is presented in Figure 12 for a temperature range of 300 K $< T <$ 503 K.

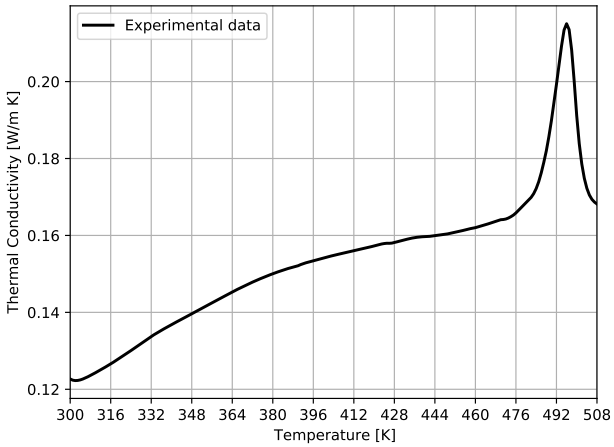

Figure 12. Thermal conductivity for the composite material as a function of temperature.

5.1.2. Optical properties

In order to obtain the emissivity, $\varepsilon_m(T_m)$, and reflectivity, $r_m(T_m)$ of the composite material as function of temperature, an in house test was designed based on the procedure indicated by pirometer manufacturers to determine the emissivity of the object being measured [50]. The results are presented in Figure 13.

Preprints (www.preprints.org) | NOT PEER-REVIEWED | Posted: 25 November 2021 doi:10.20944/preprints202109.0363.v2

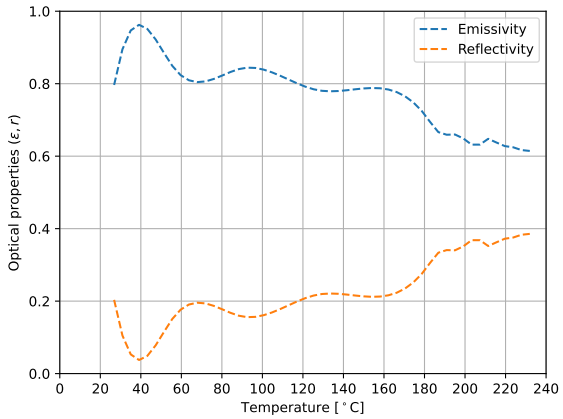

Figure 13. Emissivity and reflectivity as function of temperature for the composite material obtained by an in house test.

5.2. Methods

5.2.1. Time Integration Scheme

The mathematical model involves a set of non-linear ordinary differential equations (ODE) for the temperature time derivative of the different components namely: the tungsten filament (1), the quartz lamp (5), the reflector cells temperature (7b) and the material cells temperature (10a). To solve this ODE system the initial condition is set to be the ambient temperature for all the components. The implicit solver Radau IIA is selected from the Scientific Python library [51] to avoid time-step limitations due to equations stiffness.

The ODE equation system is structured in a array-like way to be an explicit function of the given trial temperature suitable for the external solver. To evaluate the ODE system, the following steps are performed:

Step 1. For the given trial temperature.
Step 2. Evaluate all material properties at the trial temperature.
Step 3. Solve the radiation heat flux system for the trial temperature.
Step 4. Evaluate the ODE system array with the temperature derivatives.

The model solver consists on two parts, being the first one the calculation of the net radiation flux using the current temperature as reference to determine all the properties required. The second part consists on implementing the result of the net radiation flux as input to predict the process components temperature at the next time step. Finally, the new temperatures are used to calculate a new net heat flux and the cycle repeats until the defined stop time.

The relative error tolerance for the solver is set to 10^{-4} and the absolute error tolerance to 10^{-6}.

5.2.2. Convergence analysis

A convergence analysis is performed to define a proper cell size for the material simulation in order to lower the required computational resources consumption using the lowest mesh size. Mesh sizes from 11 cells up to 239 cells were tested for the material. The mesh for the reflector is defined using the same cell size used for the material, regardless of the amount of cells, in order to preserve stability during computation. Taking into account the temperature percentage variation using as reference three selected points, namely the first cell at which the material has it's first interaction with heat exchange process, the middle cell along the length of the material, and the last cell of the material, the mesh size is selected based on the lowest number of cells which gives a temperature variation under 0.5% with respect to the mesh size of 239 cells. The number of cells defined using odd values is intended to guarantee a central cell along the mesh, at the same position, regardless the mesh size.

Preprints (www.preprints.org) | NOT PEER-REVIEWED | Posted: 25 November 2021 doi:10.20944/preprints202109.0363.v2

5.2.3. Measures and instrumentation

In order to measure the process parameters and the variables needed to feed the mathematical model, two types of data acquisition cards from National Instruments were used, namely, a NI 9234 for voltage measurements and a NI 9211 for temperature measurements. The NI 9234 data acquisition card allows high sampling rates, which is adequate to measure the 50 Hz frequency mains voltage that feeds the heating element.

To compute the electrical power delivered to the heating element, the applied voltage and the current consumption must be measured. A voltage transformer is used to step down the mains voltage sine wave to a safe range for the data acquisition card, as well as to provide galvanic isolation. For the current, a non-invasive current transformer is placed around one of the lines that powers the heating element; the output of this transformer is a voltage signal which is read by the same data acquisition card that reads the transformed mains voltage signal. The measurement strategy for voltage and current is presented in Figure 14.

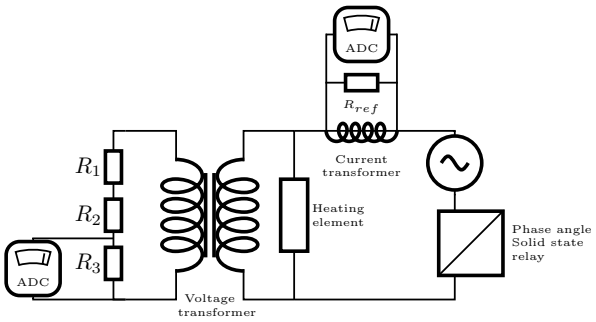

Figure 14. Voltage and current measurement strategy for electrical power consumption calculation

To measure the involved temperatures, a set of thermocuples are placed at the following locations: the compaction roll fluid inlet and outlet, and on the top surface of the mold. The composite material temperature is measured using a pyrometer PyroNFC K from CALEX facing the composite material at a point h above the center line of the compaction roll as presented in Figure 15. The output of the pyrometer is a thermocouple like signal, that can be read by the same data acquisition card, NI 9211, as the other thermocouples.

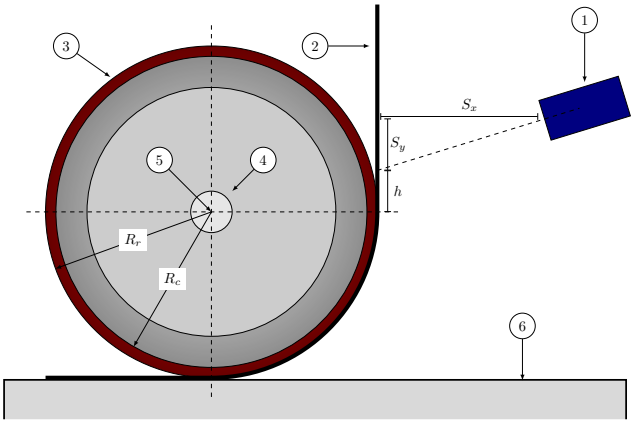

Figure 15. Composite material temperature measurement scheme. **(1)** Pyrometer PyroNFC-K. **(2)** Incoming composite material. **(3)** Compaction roll. **(4)** Compaction roll axis; fluid inlet/outlet ports. **(5)** inlet fluid temperature sensor; outlet temperature sensor located at the other end of the axis. **(6)** mold temperature sensor.

 doi:10.20944/preprints202109.0363.v2

The last parameter to measure is the process speed, this value is obtained directly as a voltage from the analogue output of the servo motor driver OMROM R88D-KN08H-ECT, being read by the NI 9234 data acquisition card.

5.2.4. Model validation

The experimental validation is performed in two parts. The first part consists on validating the temperature dynamics of the material at the measuring point as shown in Figure 15, using a constant set of parameters namely: process speed, compaction roll temperature and mold temperature, and impose changes to the voltage applied to the heating element. This voltage variation is done using a solid state relay which takes advantage of the phase angle strategy to reduce the delivered root mean square voltage, hence the electrical power delivered to the heating element.

The compaction roll temperature and the mold temperature are kept constant because any change to their respective reference generates a slow response in comparison with any change in reference for the voltage delivered to the heating element. The process speed is kept with a constant value along the experiment because the driver controlling the servo motor only has signal outputs to monitor its value, and any change will imply to stop the process and change it manually. In order to see the influence of the speed upon the process, two sets of tests are defined with different speed values, as presented in Table 3.

Table 3. Values for the process parameters

Parameter	Set 1	Set 2
Compaction roll temperature	55 °C	55 °C
Mold temperature	22 °C	22 °C
Process speed	5 mm/s	15 mm/s

To understand the machine parameters influence in the operation of the ATL head, regarding the consolidation temperature of the material tape at the nip point, the proposed test cases presented in Table 4, will be simulated.

Table 4. Values for the process simulation

Simulation	Parameters	Values
1	Compaction roll Temperature	55 °C
	Mold Temperature	22 °C
	Speed	5 mm/s
	Voltage	100 V
	Voltage	150 V
	Voltage	200 V
2	Compaction roll Temperature	55 °C
	Mold Temperature	22 °C
	Voltage	150 V
	Speed	5 mm/s
	Speed	10 mm/s
	Speed	15 mm/s

Preprints (www.preprints.org) | NOT PEER-REVIEWED | Posted: 25 November 2021 doi:10.20944/preprints202109.0363.v2

6. Results

6.1. Mesh convergence

Results for the convergence analysis are shown in Figure 16, for a speed value of 5 mm/s in Figure 16a, and for a speed value of 15 mm/s in Figure 16b, both with a simulation time of 30 seconds and the same process conditions of initial temperature and electrical power delivered to the heating element, as well as compaction roll, mold and ambient temperature.

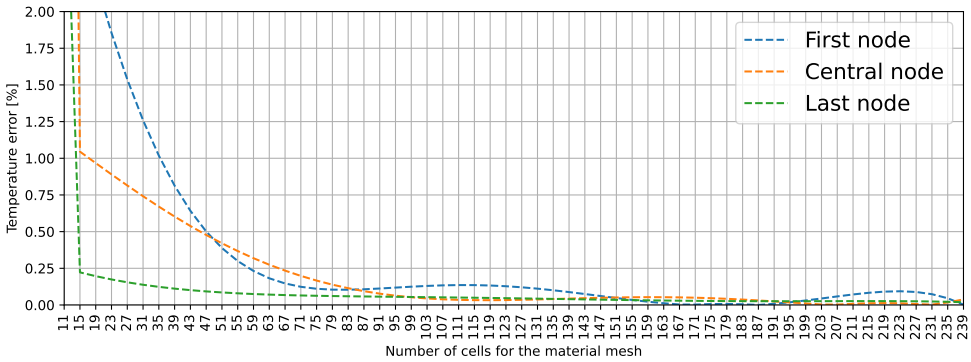

(a)

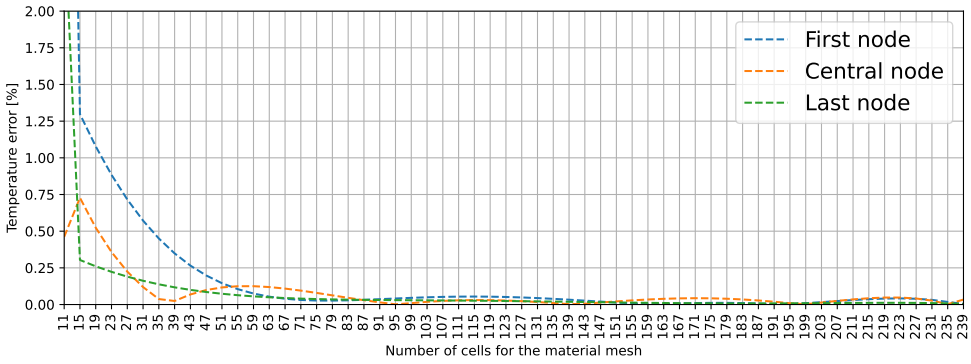

(b)

Figure 16. Temperature error as a function of the mesh size for the material. **(a)** speed value 5 mm/s. **(b)** speed value 15 mm/s.

Data presented in Figure 16a shows that for a process speed of 5 mm/s the material temperature value, at the selected locations, has a tendency to stabilize with a relative error below 0.5% for mesh sizes above 47 cells, and for the case of a process speed of 15 mm/s, the error below 0.5% is achieved with a mesh size above 35 cells. From this results, the selected mesh size is 51 cells, corresponding to the scenario presented in Figure 16a, with a cell size of $\Delta y = 2.87$ mm.

The reflector cell size is fixed to have the same size than the material, although the reflector mesh size should have less influence.

6.2. Model validation

In order to compare the dynamic response of the ATL machine with the predicted response of the proposed numerical model, different tests with multiple changes in the voltage supplied to the heating element are presented in Figure 17 and Figure 19 using the sets of fixed parameters presented in Table 3. This was done to simulate a possible control action, and to analyze the transient response of the machine and the material.

Preprints (www.preprints.org) | NOT PEER-REVIEWED | Posted: 25 November 2021 doi:10.20944/preprints202109.0363.v2

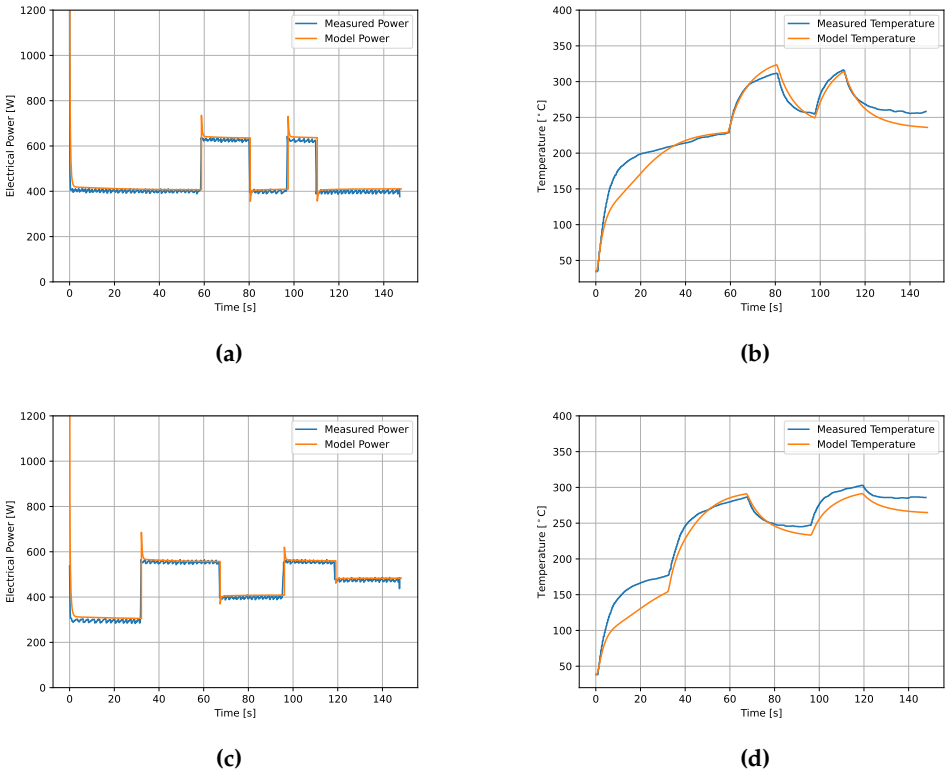

Figure 17. Results of Power consumption and temperature variation at the measuring point according to parameter set 1 from Table 3. **(a)** test 1, electrical power. **(b)** test 1, composite temperature response. **(c)** test 2, electrical power. **(d)** test 2, composite temperature response.

First, the predicted power consumption agrees with the experimental measured response as shown in Figure 17a and Figure 17c. This means that the proposed model is capable to predict the overall energy flow of the system, which is a desirable result because it is based in energy conservation laws.

Comparing the measured temperature with the predicted temperature at the corresponding "machine measurement point", it is verified that the proposed model can predict the heating and cooling dynamics of the system as shown in Figure 17b and Figure 17d according to the process speed value, compaction roll temperature and mold temperature presented in Table 3 as Set 1.

The prediction of the material temperature was adjusted by defining a compensation factor for the convection coefficient of the heating element of 5.5, correlation (41c), and a compensation factor of 2.5 for the convection coefficient of the material, correlation (42c), in order to compensate the correlations approximations related to geometry and relative movement.

Additionally, the corresponding measurements for the compaction roll temperatures, mold temperature and process speed for the test set 1 are shown in Figure 18a and Figure 18b.

Preprints (www.preprints.org) | NOT PEER-REVIEWED | Posted: 25 November 2021 doi:10.20944/preprints202109.0363.v2

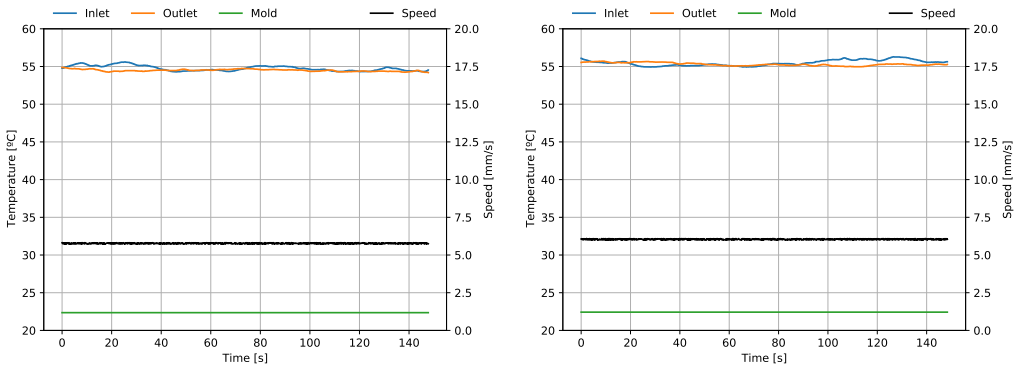

(a) **(b)**

Figure 18. Inlet and outlet compaction roll temperatures and speed measurements for two test runs, Set 1 from Table 3 **(a)** first test, refering to Figure 17a and Figure 17b. **(b)** second test, refering to Figure 17c and Figure 17d.

The test and simulation results for the process parameters presented in Table 3 as Set 2 are presented in Figure 19, showing predicted and measured power consumption for the heating element, Figure 19a and Figure 19c, and predicted and measured temperature for the material at the measuring point, Figure 19b and Figure 19d.

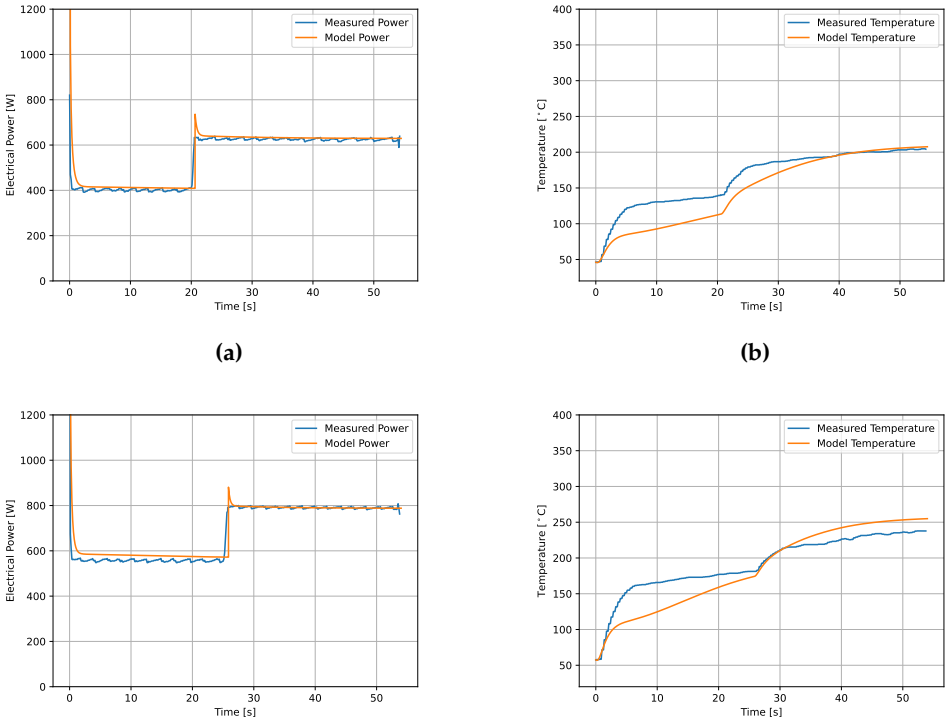

(a) **(b)**

(c) **(d)**

Figure 19. Results of Power consumption and temperature variation at the measuring point according to parameter set 2 from Table 3. **(a)** test 1, electrical power. **(b)** test 1, composite temperature response. **(c)** test 2, electrical power. **(d)** test 2, composite temperature response.

The model used to predict the composite material temperature at the machine measuring point shown in Figure 19b and Figure 19d includes the same compensation factors in the convection coefficient for the heating element as well as in the material convection coefficient, showing an acceptable geometrical and relative movement compensation for those values.

Preprints (www.preprints.org) | NOT PEER-REVIEWED | Posted: 25 November 2021 doi:10.20944/preprints202109.0363.v2

The corresponding measurements for the compaction roll temperature, mold temperature and process speed are shown in Figure 20.

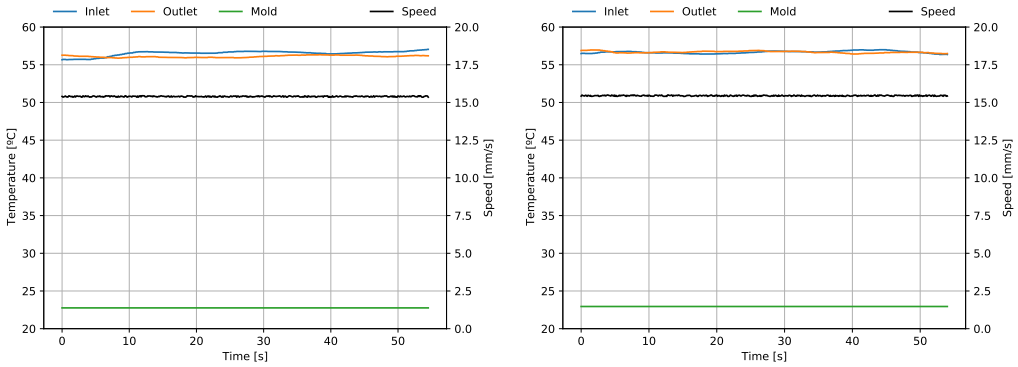

(a) **(b)**

Figure 20. Inlet and outlet compaction roll temperatures and speed measurements for two test runs, Set 2 from Table 3. **(a)** first test, refering to Figure 19a and Figure 19b. **(b)** second test, refering to Figure 19c and Figure 19d.

As shown in Figure 17b, Figure 17d, Figure 19b and Figure 19d, the model is capable of predict the temperature of the material for values above 150 °C (423.15 K).

Comparing the measured temperatures at the same machine measuring point for both process speeds, it is noticed that when defining a machine speed of 15 mm/s, temperatures at this point are lower than the temperatures at the same point when tests are performed with a machine speed of 5 mm/s, showing the influence of the transport phenomena upon the temperature evolution along time.

It can be seen that the compaction roll inlet and outlet temperatures are similar at both tests, this fact added to an internal fluid flow through the compaction roll of 40 l/min produced by a temperature control unit Tool-Temp 137BP, indicates that the internal flow is enough to guarantee a constant temperature along the compaction roll, validating the proposed model assumption of constant temperature given in section 3.4.

Figure 21 presents the prediction of the Nip Point temperature, related to the measured tests presented in Figure 17b and Figure 17d. A delay between the nip point temperature change and the predicted temperature at the measured point can be noticed in Figure 15, when simulating the change in voltage of the heating element by a control system while the process speed remains constant.

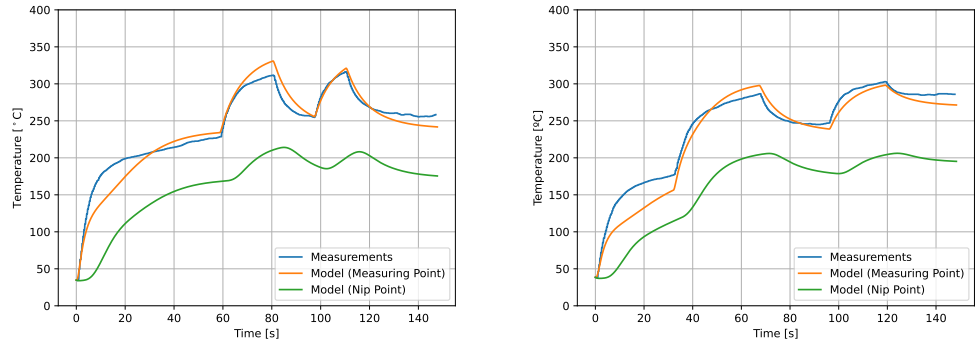

(a) **(b)**

Figure 21. Temperature at measuring point, predicted at measuring point and predicted at Nip Point. **(a)** first measured test. **(b)** second measured test

This result is expected and is related to the transport phenomena due to the feed speed, and the heat conduction to the roll.

Preprints (www.preprints.org) | NOT PEER-REVIEWED | Posted: 25 November 2021 doi:10.20944/preprints202109.0363.v2

6.2.1. Sensitivity analysis

The results for the simulations described in Table 4 are presented in Figure 22 for the simulation in which the speed of the process is kept constant (Simulation 1), and in Figure 23 for the simulation in which the voltage applied to the heating element is kept constant (Simulation 2).

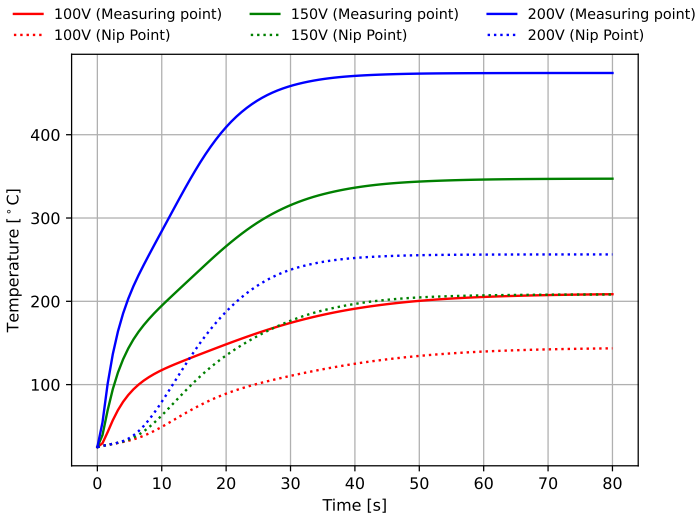

Figure 22. Results for the simulations according to the first simulation proposed in Table 4

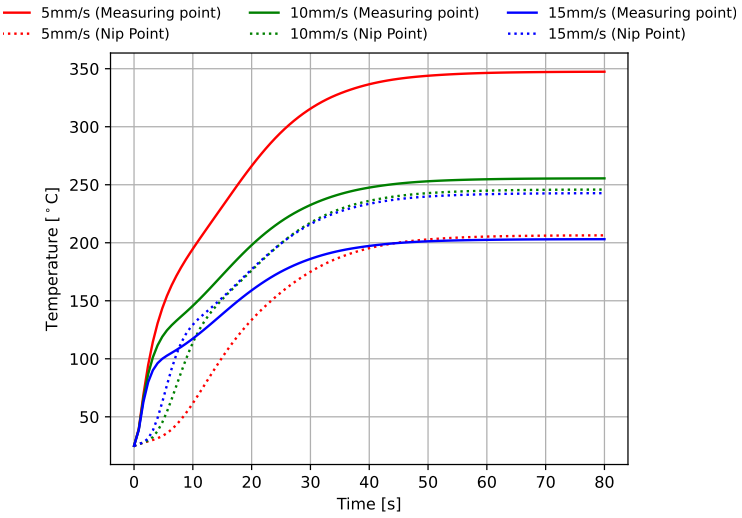

Figure 23. Results for the simulations according to the second simulation proposed in Table 4

For the case presented in Figure 22, the temperature at the nip point also presents a delay with respect to the measuring point as expected, and is controlled by ambient losses and the heat transferred to the roll. Figure 23 shows that the process speed has a relevant influence on the nip point temperature as its value increases, this effect that can be noticed for the simulated speed of 10 mm/s, where after the nip point temperature starts to rise, it almost matches the temperature of the measuring point, and for the case of a speed of 15 mm/s the temperature experiences a start delay and rapidly reaches higher values with respect to the measuring point. This behaviour demonstrates the high sensitivity of the system to the feed speed, meaning that the transport phenomena dominates over the conduction and convection losses.

7. Conclusions

The energy balance model proposed for the heating element is able to replicate the dynamics of its electrical energy consumption, taking into account its components properties and geometrical parameters. It is also capable of predicting the outgoing energy flux towards the material being processed causing the temperature to raise along the material length.

The compaction roll can be modelled assuming isothermal conditions along its internal fluid section by ensuring a sufficient fluid flow, causing a temperature gradient along the compaction roll thickness. This assumption simplifies the heat transfer model at this element.

The proposed 1.5D heat transfer model for the automated tape laying machine head, can be used to simulate the temperature distribution along the processed material, and its dynamics upon changes on the heating element input voltage and process speed, predicting the temperature along the heating zone domain.

The most relevant parameters that influence the machine behavior are the input voltage of the heating element that increases the temperature of the processed composite material by directly heating its surface using radiation, and the process speed that influences the material temperature by the transport effects.

The current machine configuration has an appropriate design, being capable of raising the material temperature to the required consolidation temperature value, if a suitable control system is implemented.

With this model, that takes into account the thermal and optical properties of the material involved, and their changes with temperature, a digital twin of the process can be formulated to develop control strategies using the machine head speed and the lamp power as the variables manipulated in order to control the nip point temperature. This model also allows to estimate the composite temperature profile along the heating zone, acting as a supervisory function for a control system allowing it to handle imposed constraints related to the material.

As the digital twin of the process is capable of estimating the composite temperature at the nip point, it lends to create a temperature registry along time for further thermo-mechanical analysis in order to analyze defects due to residual stress.

The digital twin model can be used for selecting the best process elements and their capabilities in terms of the heat source delivering capabilities, the process speed and the mold temperature as a function of the composite material being processed in order to meet quality requirements of the final product. So, the study of those effects on an already built machinecan be avoided, with large time and economic benefits.

Author Contributions: Conceptualization, J.R. and P.G.; methodology, J.R. and P.G; software, J.R.; validation, J.R.; formal analysis, J.R. and P.G.; investigation, J.R.; resources, J.R.; data curation, J.R.; writing—original draft preparation, J.R. and P.G.; writing—review and editing, J.R., P.G., L.P. and F.G.A; visualization, J.R.; supervision, L.P. and F.G.A; project administration, J.R.; funding acquisition, J.R. All authors have read and agreed to the published version of the manuscript.

Funding: This research has received funding from the European Union's Horizon 2020 research and innovation programme under grant agreement No 768710.

Conflicts of Interest: The authors declare no conflict of interest.

References

1. Engelhardt, R.; Ehard, S.; Wolf, T.; Oelhafen, J.; Kollmannsberger, A.; Drechsler, K. In Situ Joining of Unidirectional Tapes on Long Fiber Reinforced Thermoplastic Structures by Thermoplastic Automated Fiber Placement for Scientific Sounding Rocket Applications. *Procedia CIRP* **2019**, *85*, 189–194. doi:10.1016/j.procir.2019.09.015.
2. Comer, A.J.; Ray, D.; Obande, W.O.; Jones, D.; Lyons, J.; Rosca, I.; O'Higgins, R.M.; McCarthy, M.A. Mechanical characterisation of carbon fibre-PEEK manufactured by laser-assisted automated-tape-placement and autoclave. *Composites Part A: Applied Science and Manufacturing* **2015**, *69*, 10–20. doi:10.1016/j.compositesa.2014.10.003.

3. Saenz-Castillo, D.; Martín, M.; Calvo, S.; Rodriguez-Lence, F.; Güemes, A. Effect of processing parameters and void content on mechanical properties and NDI of thermoplastic composites. *Composites Part A: Applied Science and Manufacturing* **2019**, *121*, 308–320. doi:10.1016/j.compositesa.2019.03.035.
4. Barakat, E.; Tannous, M. Simulation of the tape laying process with steering of tapes: Bonding defects prevention using simulation. 2019 Fourth International Conference on Advances in Computational Tools for Engineering Applications (ACTEA). IEEE, 2019, pp. 1–7. doi:10.1109/ACTEA.2019.8851111.
5. Crosky, A.; Grant, C.; Kelly, D.; Legrand, X.; Pearce, G. Fibre placement processes for composites manufacture. In *Advances in Composites Manufacturing and Process Design*; Elsevier, 2015; pp. 79–92. doi:10.1016/B978-1-78242-307-2.00004-X.
6. Khan, M.A.; Mitschang, P.; Schledjewski, R. Identification of some optimal parameters to achieve higher laminate quality through tape placement process. *Advances in Polymer Technology* **2010**, *29*, 98–111. doi:10.1002/adv.20177.
7. Liebsch, A.; Koshukow, W.; Gebauer, J.; Kupfer, R.; Gude, M. Overmoulding of consolidated fibre-reinforced thermoplastics - increasing the bonding strength by physical surface pre-treatments. *Procedia CIRP* **2019**, *85*, 212–217. doi:10.1016/j.procir.2019.09.047.
8. Tumkor, S.; Turkmen, N.; Chassapis, C.; Manoochehri, S. Modeling of heat transfer in thermoplastic composite tape lay-up manufacturing. *International Communications in Heat and Mass Transfer* **2001**, *28*, 49–58. doi:10.1016/S0735-1933(01)00212-3.
9. Martín, M.; Rodríguez-Lence, F.; Güemes, A.; Fernández-López, A.; Pérez-Maqueda, L.; Perejón, A. On the determination of thermal degradation effects and detection techniques for thermoplastic composites obtained by automatic lamination. *Composites Part A: Applied Science and Manufacturing* **2018**, *111*, 23–32. doi:10.1016/j.compositesa.2018.05.006.
10. Parlevliet, P.P.; Bersee, H.E.; Beukers, A. Residual stresses in thermoplastic composites - a study of the literature. Part III: Effects of thermal residual stresses. *Composites Part A: Applied Science and Manufacturing* **2007**, *38*, 1581–1596. doi:10.1016/j.compositesa.2006.12.005.
11. Sonmez, F.O.; Hahn, H.T. Modeling of Heat Transfer and Crystallization in Thermoplastic Composite Tape Placement Process. *Journal of Thermoplastic Composite Materials* **1997**, *10*, 198–240. doi:10.1177/089270579701000301.
12. Stokes-Griffin, C.M.; Compston, P.; Matuszyk, T.I.; Cardew-Hall, M.J. Thermal modelling of the laser-assisted thermoplastic tape placement process. *Journal of Thermoplastic Composite Materials* **2015**, *28*, 1445–1462. doi:10.1177/0892705713513285.
13. Schaefer, P.M.; Gierszewski, D.; Kollmannsberger, A.; Zaremba, S.; Drechsler, K. Analysis and improved process response prediction of laser- assisted automated tape placement with PA-6/carbon tapes using Design of Experiments and numerical simulations. *Composites Part A: Applied Science and Manufacturing* **2017**, *96*, 137–146. doi:10.1016/j.compositesa.2017.02.008.
14. Khan, M.A.; Mitschang, P.; Schledjewski, R. Tracing the Void Content Development and Identification of its Effecting Parameters during in Situ Consolidation of Thermoplastic Tape Material. *Polymers and Polymer Composites* **2010**, *18*, 1–15. doi:10.1177/096739111001800101.
15. Stokes-Griffin, C.; Compston, P. A combined optical-thermal model for near-infrared laser heating of thermoplastic composites in an automated tape placement process. *Composites Part A: Applied Science and Manufacturing* **2015**, *75*, 104–115. doi:10.1016/j.compositesa.2014.08.006.
16. Hosseini, S.M.A.; Baran, I.; van Drongelen, M.; Akkerman, R. On the temperature evolution during continuous laser-assisted tape winding of multiple C/PEEK layers: The effect of roller deformation. *International Journal of Material Forming* **2020**. doi:10.1007/s12289-020-01568-7.
17. Pitchumani, R.; Gillespie, J.W.; Lamontia, M.A. Design and Optimization of a Thermoplastic Tow-Placement Process with In-Situ Consolidation. *Journal of Composite Materials* **1997**, *31*, 244–275. doi:10.1177/002199839703100302.
18. Lichtinger, R.; Hörmann, P.; Stelzl, D.; Hinterhölzl, R. The effects of heat input on adjacent paths during Automated Fibre Placement. *Composites Part A: Applied Science and Manufacturing* **2015**, *68*, 387–397. doi:10.1016/j.compositesa.2014.10.004.
19. Belnoue, J.P.; Mesogitis, T.; Nixon-Pearson, O.J.; Kratz, J.; Ivanov, D.S.; Partridge, I.K.; Potter, K.D.; Hallett, S.R. Understanding and predicting defect formation in automated fibre placement pre-preg laminates. *Composites Part A: Applied Science and Manufacturing* **2017**, *102*, 196–206. doi:10.1016/j.compositesa.2017.08.008.
20. Colton, J.; Leach, D. Processing parameters for filament winding thick-section PEEK/carbon fiber composites. *Polymer Composites* **1992**, *13*, 427–434. doi:10.1002/pc.750130605.
21. Di Francesco, M.; Veldenz, L.; Dell'Anno, G.; Potter, K. Heater power control for multi-material, variable speed Automated Fibre Placement. *Composites Part A: Applied Science and Manufacturing* **2017**, *101*, 408–421. doi:10.1016/j.compositesa.2017.06.015.
22. Silex. Silicone Rubber Sheeting High Temperature Solid, Datasheet, 2019.
23. Narnhofer, M.; Schledjewski, R.; Mitschang, P.; Perko, L. Simulation of the Tape-Laying Process for Thermoplastic Matrix Composites. *Advances in Polymer Technology* **2013**, *32*, E705–E713. doi:10.1002/adv.21312.
24. Chinesta, F.; Leygue, A.; Bognet, B.; Ghnatios, C.; Poulhaon, F.; Bordeu, F.; Barasinski, A.; Poitou, A.; Chatel, S.; Maison-Le-Poec, S. First steps towards an advanced simulation of composites manufacturing by automated tape placement. *International Journal of Material Forming* **2014**, *7*, 81–92. doi:10.1007/s12289-012-1112-9.
25. Pettersson, M.; Stenström, S. Modelling of an electric IR heater at transient and steady state conditions: Part I: model and validation. *International Journal of Heat and Mass Transfer* **2000**, *43*, 1209–1222.
26. Incropera, F.P.; DeWitt, D.P.; Bergman, T.L.; Lavine, A.S. *Fundamentals of Heat and Mass Transfer 6th Edition*; JOHN WILEY & SONS, 2007. doi:10.1016/j.applthermaleng.2011.03.022.
27. Howell, J.; Menguc, M.; Siegel, R. *Thermal Radiation Heat Transfer*; CRC Press, 2015.
28. Modest, M. *Radiative Heat Transfer*, 3rd editio ed.; Academic Press, 2013; p. 904.

29. Shapiro, a. FACET: a radiation view factor computer code for axisymmetric, 2D planar, and 3D geometries with shadowing. *BioTechniques* **1983**, *38*.
30. Pettersson, M. *Heat Transfer and Energy Efficiency in Infrared Paper Dryers*; Number december, Chemical Engineering, Lund University, 1999.
31. Forsythe, W.E.; Adams, E.Q. Radiating Characteristics of Tungsten and Tungsten Lamps A Correction. *Journal of the Optical Society of America* **1945**, *35*, 306. doi:10.1364/josa.35.000306.
32. Izuegbu, N.S.; Adonis, M.L. Simulation and modelling of energy efficient design of a ceramic infrared heater. *2011 Proceedings of the 8th Conference on the Industrial and Commercial Use of Energy, ICUE 2011* **2011**, pp. 69–74.
33. Lampinen, M.J.; Ojala, K.T.; Koski, E. MODELING AND MEASUREMENTS OF INFRARED DRYERS FOR COATED PAPER. *Drying Technology* **1991**, *9*, 973–1017. doi:10.1080/07373939108916730.
34. Venkateshan, S. *Heat Transfer*; Springer International Publishing: Cham, 2021; pp. 160–189. doi:10.1007/978-3-030-58338-5.
35. Feingold, A.; Gupta, K.G. New analytical approach to the evaluation of configuration factors in radiation from spheres and infinitely long cylinders. *Journal of Heat Transfer* **1970**, *92*, 69–6. doi:10.1115/1.3449647.
36. Domalski, E.S. NIST Chemistry WebBook, 2011.
37. Bansal, N.P. *Handbook of Glass Properties*; Elsevier, 1986; p. 680. doi:10.1016/C2009-0-21785-5.
38. Sergeev, O.A.; Shashkov, A.G.; Umanskii, A.S. Thermophysical properties of quartz glass. *Journal of Engineering Physics* **1982**, *43*, 1375–1383. doi:10.1007/BF00824797.
39. Chase, M.W.; Curnutt, J.L.; Downey, J.R.; McDonald, R.A.; Syverud, A.N.; Valenzuela, E.A. JANAF Thermochemical Tables, 1982 Supplement. *Journal of Physical and Chemical Reference Data* **1982**, *11*, 695–940. doi:10.1063/1.555666.
40. Gale, W.F.; Totemeier, T.C. *Smithells metals reference book*, 8th ed.; Vol. 1, Elsevier, 2003; p. 2080.
41. CRC Handbook of Chemistry and Physics, 84th Edition Edited by David R. Lide (National Institute of Standards and Technology). CRC Press LLC: Boca Raton. 2003. 2616 pp. $139.95. ISBN 0-8493-0484-9. *Journal of the American Chemical Society* **2004**, *126*, 1586–1586. doi:10.1021/ja0336372.
42. Hust, J.G.; Lankford, A.B. *Thermal Conductivity of Aluminium, Copper, Iron, and Tungsten for Temperatures from 1 K to the Melting Point*; Number June, U.S. Department of Commerce, 1984; p. 266.
43. Edwards, T.C.; Steer, M.B. *Foundations for microstrip circuit design*, fourth edi ed.; John Wiley & Sons, 2016.
44. Toray Group. Nylon 6-based Thermoplastic Composite, 2019.
45. ASTM E 1269-9901 - Standard Test Method for Determining Specific Heat Capacity by Differential Scanning Calorimetry, 2001.
46. Zhai, S.; Zhang, P.; Xian, Y.; Zeng, J.; Shi, B. Effective thermal conductivity of polymer composites: Theoretical models and simulation models. *International Journal of Heat and Mass Transfer* **2018**, *117*, 358–374. doi:10.1016/j.ijheatmasstransfer.2017.09.067.
47. Villière, M.; Lecointe, D.; Sobotka, V.; Boyard, N.; Delaunay, D. Experimental determination and modeling of thermal conductivity tensor of carbon/epoxy composite. *Composites Part A: Applied Science and Manufacturing* **2013**, *46*, 60–68. doi:10.1016/j.compositesa.2012.10.012.
48. Betta, G.; Rinaldi, M.; Barbanti, D.; Massini, R. A quick method for thermal diffusivity estimation: Application to several foods. *Journal of Food Engineering* **2009**, *91*, 34–41. doi:10.1016/j.jfoodeng.2008.08.003.
49. Yang, C.Y. Estimation of the temperature-dependent thermal conductivity in inverse heat conduction problems. *Applied Mathematical Modelling* **1999**, *23*, 469–478. doi:10.1016/S0307-904X(98)10093-8.
50. Optris. Compact IR pyrometer for OEM applications: optris CS LT, 2021.
51. Hairer, E.; Wanner, G. *Solving Ordinary Differential Equations II*; Vol. 14, *Springer Series in Computational Mathematics*, Springer Berlin Heidelberg: Berlin, Heidelberg, 1996. doi:10.1007/978-3-642-05221-7.